

# Spatially Resolved Colors and Stellar Population Properties in Early-Type Galaxies at $z \sim 1.5$ .

A. Gargiulo<sup>1\*</sup>, P. Saracco<sup>1</sup>, M. Longhetti<sup>1</sup>, F. La Barbera<sup>2</sup>, S. Tamburri<sup>1,3</sup>

<sup>1</sup>*INAF-Osservatorio Astronomico di Brera, via Brera 28, 20121 Milano, Italy*

<sup>2</sup>*INAF-Osservatorio Astronomico di Napoli, salita Moiarriello 16, 80121 Napoli, Italy*

<sup>3</sup>*Università degli Studi dell'Insubria, via Valleggio 11, 22100 Como, Italy*

Accepted 2012 July 5. Received 2012 June 13; in original form 2012 March 26

## ABSTRACT

We present F850LP-F160W color gradients for 11 early-type galaxies (ETGs) at  $1.0 < z_{spec} < 1.9$  selected from the GOODS South field. Significant negative F850LP-F160W color gradients (core redder than the outskirts) have been detected in  $\sim 70\%$  of our sample within the effective radius  $R_e$ , the remaining 30% having a flat color profile consistent with a null gradient. Extending the analysis at  $R > R_e$ , enclosing the whole galaxy, we have found that the fraction of high- $z$  ETGs with negative F850LP-F160W color gradients rises up to 100%. For each galaxy, we investigate the origin of the radial color variation with an innovative technique based on the matching of both the spatially resolved color and the global spectral energy distribution (SED) to predictions of composite stellar population models. In fact, we find that the age of the stellar populations is the only parameter whose radial variation alone can fully account for the observed color gradients and global SEDs for half of the galaxies in our sample (6 ETGs), without the need of radial variation of any other stellar population property. For four out of these six ETGs, a pure metallicity variation can also reproduce the detected color gradients. Nonetheless, a minor contribution to the observed color gradients from radial variation of star-formation time scale, abundance of low-to-high mass stars and dust cannot be completely ruled out. For the remaining half of the sample, our analysis suggests a more complex scenario whereby more properties of the stellar populations need to simultaneously vary, likely with comparable weights, to generate the observed color gradients and global SED. Our results show that, despite the young mean age of our galaxies ( $< 3-4$  Gyr), they already exhibit significant differences among their stellar content. We have discussed our results within the framework of the widest accepted scenarios of galaxy formation and conclude that none of them can satisfactorily account for the observed distribution of color gradients and for the spatially resolved content of high- $z$  ETGs. Our results suggest that the distribution of color gradients may be due to ETGs forming by different mechanisms.

**Key words:** galaxies: elliptical and lenticular, cD galaxies: evolution galaxies: formation galaxies: high-redshift galaxies: stellar content.

## 1 INTRODUCTION

A viable way to gather insight on the processes that concur to accrete the stellar mass in early-type galaxies (ellipticals plus S0's, hereafter ETGs) is to analyze the spatial distribution and properties of their stellar content which, in principle, can be directly connected to the events experienced by the galaxies. Indeed, the different scenarios proposed to

explain the formation of ETGs give different predictions on their stellar population content.

The *revised* monolithic model predicts that, in a cold dark matter framework, massive ETGs assemble the bulk of their mass at  $z > 2-3$  through the merger of small substructures moving in a common potential well. This initial collapse might be regulated by cold gas streams from the cosmological surroundings, also known as cold accretion (Dekel et al. 2009), the latter becoming less important, for high-mass galaxies, at lower redshift. The subsequent evolution should be mainly characterized by the aging of

\* E-mail: adriana.gargiulo@brera.inaf.it

their stellar populations, with small new episodes of star-formation at  $z < 1$ , related, e.g., to the capture of satellites (Katz 1991; Kawata 2001; Kobayashi 2004; Merlin & Chiosi 2006). During the gravitational dissipative collapse, the metal-enriched gas should naturally flow towards the center of the galaxy, leading to an ETG with stellar populations more metal-rich in the center than in the external regions (i.e. negative metallicity gradient). Moreover, because of the deeper potential well, the star-formation is expected to last longer in the central than in the outer regions. This would lead to null or mildly positive age gradients, with stellar populations in the center  $\sim 10\%$  younger than those in the outskirts (Kobayashi 2004). Nonetheless the effect of metallicity variation on color profile should be the dominant one, thus in this scenario ETGs are generally expected with negative color gradients.

The competing formation scheme is the *hierarchical* scenario. Following the hierarchical assembly of cosmic structures, ETGs are supposed to form through gas-rich (“wet”) mergers of disc galaxies (e.g. Toomre & Toomre 1972; De Lucia et al. 2006) at high-redshift ( $z \sim 4-5$ ). In this phase, a large fraction of the stellar mass of a galaxy is assembled through central intense bursts of star formation (e.g. Renzini 2006). Concurrently, a “dry” merger picture has also been advocated, where bright ETGs would form through the merging of quiescent galaxies (e.g. Bell et al. 2004). Actually, in the last years a new scheme of mass accretion of massive ETGs, known as *inside-out growth*, is becoming widely accepted. This scenario is motivated by the observational evidence of ETGs at  $1.0 < z < 2.5$  with effective radii 3-5 times smaller than the mean radius of local ETGs with the same stellar mass (e.g. Daddi et al. 2005; Longhetti et al. 2007). In this context, supported by a wealth of simulations (e.g. Khochfar & Silk 2006; Hopkins et al. 2009; Wuyts et al. 2010; Naab et al. 2009; Bezanson et al. 2009) ETGs are supposed to be formed at high redshift ( $z \sim 4-5$ ) as compact spheroids result of gas-rich mergers. Then, at lower redshift, compact ETGs would undergo subsequent minor-“dry” mergers, whose main effect is to add an external low-mass density envelope to the compact core ETGs, enlarging the effective radius while leaving the stellar mass nearly constant. Indeed, this scenario shows some limitations, such as the not plausible number of minor-“dry” mergers necessary to enlarge the ETGs’ size which could produce a scatter in the fundamental plane much larger than the observed one, and its failure to explain the presence of normal ETGs observed at high- $z$  in number similar to the compact ones (e.g. Nipoti et al. 2009; Saracco et al. 2011, 2010). From a theoretical point of view, the “wet”-merger scenario predicts ETGs with significant radial age variations. Indeed, the galaxy remnant of a wet merger should be characterized by a central stellar population younger, and more metal-rich, than the outer one, i.e. by a positive (negative) age (metallicity) gradient (Kobayashi 2004). On the contrary, “dry”-mergers, mixing the pre-existing stellar populations of progenitor galaxies, should dilute any radial variation of age and metallicity, producing flatter distributions (but see also Di Matteo et al. (2009)). In the *inside-out* scenario minor dry-mergers are actually believed to only *add* an *outer* low-density envelope on top of a compact core, without mixing the pre-existing stellar-populations but redistributing the star content of the satellites in the outer regions of the

compact ETG.

The picture described so far shows how important can be to spatially resolve the properties of the underlying stellar populations of ETGs in order to pinpoint their formation scenario. The most viable way to carry out information on the radial variation of the stellar content of a galaxy is to investigate its radial color variation, being the color of a stellar population tightly dependent on its age, star-formation time scale, metallicity, and (eventual) presence of dust. ETGs at high redshift (hereafter with “high redshift” we mean  $z > 1$ ) represent the best-suited benchmark to investigate and constrain the mechanisms driving the mass assembly of spheroids due to the short time elapsed since their formation. So far, instrumental limits have allowed only studies of the global (i.e. integrated) properties of high- $z$  spheroids, preventing, indeed, any measure of their spatially resolved information. Recently, the capabilities of the Hubble Space Telescope (HST) have made possible to overwhelm part of these limitations for the first time. Gargiulo et al. (2011, hereafter GSL11) taking advantage of the deep and high-resolution HST Advanced Camera for Surveys (HST/ACS) images of the GOODS South field derived F606W - F850LP color gradients ( $\sim (UV-U)_{restframe}$  at  $z=1.5$ ,  $\lambda_{eff}$  of F606W and F850LP filter  $\sim 5810 \text{ \AA}$  and  $9010 \text{ \AA}$  respectively) for 20 ETGs at  $1 < z_{spec} < 2$ . In their work they ascertained the feasibility of this analysis up to  $z \sim 2$  and presented the first spatially resolved information for ETGs at high- $z$ . Despite the short wavelength baseline covered,  $\sim 50\%$  of the galaxies showed a significant (positive or negative) color gradient. These results clearly showed that, after 3-4 Gyr (at most) from their birth, ETGs do not exhibit a unique spatial distribution of their stellar populations, implying that they followed different mass assembly paths. Unfortunately, the available HST data, mainly optical, prevented the authors to discriminate the drivers of the observed color gradients (e.g. radial variations of age, metallicity, ...) and consequently, to constrain the mechanisms responsible for them. Indeed, at  $\langle z \rangle \sim 1.5$ , the galaxy emission sampled by the F606W and F850LP filters is sensitive to both age and dust variation. Moreover, it is dominated by the youngest ( $\sim 1\text{Gyr}$ ) stellar populations, missing any information on the distribution of the oldest stellar populations.

The recent advent of the first HST Wide Field Camera 3 (HST/WFC3) near infrared images for part of the GOODS South area (see Section 2 for details) has opened new possibilities to study color gradients of high- $z$  ETGs and to constrain their origin. In this paper we combine the information provided by the WFC3/F160W-band ( $\sim R$ -band rest-frame at  $\langle z \rangle \sim 1.5$ ,  $\lambda_{eff}$  of the filter  $\sim 15369 \text{ \AA}$ ) and F850LP-band emission to derive the F850LP-F160W color gradients ( $\sim (U-R)_{restframe}$  at  $z=1.5$ ) for a sample of 11 ETGs at  $\langle z \rangle \sim 1.5$ . The bands we selected sample emissions dominated by different stellar populations. In particular, differently from F606W-F850LP color, the F850LP-F160W color is much more sensitive to age variations than dust content. This allows us to extend and to complement the analysis presented by GSL11.

Actually, Guo et al. (2011) presented F850LP-F160W color gradients for 4 massive passively evolving galaxies in the GOODS South area at  $1.3 < z_{spec} < 2$ . They derived the color profiles by measuring optical-NIR colors in concentric annuli, and found that high- $z$  ETGs have cores redder than

the outskirts. The observed radial trend in color gradients is not reproduced by the radial variation of a single stellar population parameter (age, metallicity, extinction), although they found that dust should partially contribute to generate the observed color distribution. In this paper, we examine a sample three times larger than that of Guo et al. (2011), deriving F850LP-F160W color profiles from the 2-dimensional fit of the light profiles in the two bands. Then, we present a new approach to exploit the wealth of available information to constrain the radial variation of the underlying stellar populations. In fact, taking advantage of a unique set of data and an innovative procedure, we are able to constrain the radial variation of stellar population parameters (age, metallicity, dust, star-formation time scale, and initial mass function) and their contribution to produce the color gradients we observe in high- $z$  ETGs. Finally, we compare our findings to the prediction of theoretical formation models.

Throughout the paper we adopt a standard  $\Lambda$ CDM cosmology with  $H_0=70\text{km s}^{-1}\text{Mpc}^{-1}$ ,  $\Omega_m=0.3$  and  $\Omega_\Lambda=0.7$ . All the magnitudes are in the AB system.

## 2 THE SAMPLE

We have derived F850LP-F160W color gradients for 11 ETGs at  $\langle z \rangle \sim 1.5$ . The sample has been extracted from the complete sample of 34 ETGs selected on the whole GOODS South field (GOODS-South v2; Giavalisco et al. 2004) and presented in Saracco et al. (2010). The morphological classification was performed by the authors both on the basis of a visual inspection of the F850LP images and of Sersic index  $n_{F850LP}$  ( $n_{F850LP} > 2$ ). Starting from this complete sample we have restricted our preliminary analysis to those ETGs with near-IR WFC3 data (16 ETGs out of 34). Indeed, as pointed out in the Introduction, two areas of the GOODS South field have been imaged in the F160W band with the WFC3 extending the space-based data from the pre-existing optical domain to the near-infrared one. The Early Release Science (ERS, propID: 11359, PI: R. W. O’Connell) imaged an area of  $\sim 40$  arcmin<sup>2</sup>. Briefly, the observations were acquired with a 2-cycles-long exposures for a total exposure time of  $\sim 6$  ks, reaching a  $5\sigma$  depth in the AB system of  $F160W = 27.25$  (Windhorst et al. 2011). Additionally, the HUDF09 HST Treasury program (GO 11563, PI: Illingworth) provides the first ultra-deep near-IR WFC3 observation of the Hubble Ultra Deep Field (HUDF). The images cover an area of  $\sim 4.7$  arcmin<sup>2</sup>. At the time of our analysis, the first epoch data were available for a total exposure time of  $\sim 80$  ks and a depth at  $5\sigma$  of 28.8 in the F160W filter (AB magnitude, Oesch et al. 2010). Starting from the raw WFC3 images, we have created the mosaic images with the software MULTIDRIZZLE (Koekemoer et al. 2002) reducing the pixel/scale of the mosaic from the original value of 0.128 "/px to 0.06 "/px. In the final mosaics we have stacked only those single exposures not affected by the presence of persistence. Thus, we have obtained the WFC3/F160W-band mosaics of the ERS and HUDF09 area. Both mosaics are characterized by a full width at half maximum (FWHM) of  $\sim 0.2''$ . The exposure times are  $\sim 80$  ks and  $\sim 6$  ks for the HUDF09 and ERS, respectively.  $S/N > 5$  at  $3r_e$  are reached for the faintest galaxies of our sample in

the ERS area, the one with lower exposure time. This  $S/N$  and the resolution of the WFC3 assure us reliable estimates of the surface brightness parameters even in the images with the shorter exposure time (see Sec. 3.1).

Out of the 16 ETGs with NIR WFC3 data available, five objects have been excluded from the present analysis because of either potential problems in the modelling of the near-IR galaxy light distribution (4 ETG, Sec. 3), or of large uncertainties in the estimate of their structural parameters (1 ETG, Sec. 3.1). These selections result into a final sample of 11 galaxies. Each one of these galaxies is provided with spectroscopic redshift (Vanzella et al. 2008 and references therein) and with the wide photometric coverage of the GOODS survey: four deep HST/Advanced Camera for Surveys (ACS) images in the F435W, F606W, F775W, F850LP bands, extensive observations with ESO telescopes both in three optical U bands and with J, H,  $K_s$  near-infrared filters and four *Spitzer*-IRAC images in the 3.6, 4.5, 5.8, 8.0 $\mu$ m bands. Morphological parameters (effective radius and Sersic index) in the F850LP filter and physical parameters (age and stellar mass) were already estimated for each galaxy of the sample (Saracco et al. 2010). Four out of the 11 ETGs were already studied in GSL11, thus F606W-F850LP color gradients are also available (GSL11).

## 3 SURFACE BRIGHTNESS PARAMETERS ESTIMATION

Following GSL11, we have estimated the internal color gradient of a galaxy as the logarithmic slope of its color profile, given by the difference between the  $\mu_{F850LP}(r)$  and  $\mu_{F160W}(r)$  surface brightness profiles. As for the F850LP and F606W bands, we have modelled the F160W surface brightness profile of high- $z$  ETGs with a Sersic law:

$$\mu(R) = \mu_e + \frac{2.5b_n}{\ln(10)} [(r/r_e)^{1/n} - 1]. \quad (1)$$

To estimate the free parameters of the profile, i.e. the effective radius  $r_e$  (in units of arcsec), the Sersic index  $n$ , and the normalization term  $\mu_e$ , we have used GALFIT (v2, Peng et al. 2002). This software models the galaxy light distribution with a two-dimensional fit. In the fitting procedure, the galaxy model is convolved with the PSF, provided by the user, and the software retains as final solution the parameters of the PSF-convolved model that minimizes the residuals to the input galaxy image. For each galaxy, we have constructed different PSF models, each model being obtained by averaging the light profiles of unsaturated stars as near as possible to the position of the given galaxy on the frame. We have run GALFIT for all different PSFs and have retained the case that returns the best residual map (i.e. flat-test residuals). For four out of 16 initially selected galaxies, we found significant substructures in the residual maps, possibly indicating an inaccurate modeling of the galaxy light distribution and/or of the PSF. We have excluded these four galaxies from the analysis (see Sec. 2).

### 3.1 Robustness of structural parameter estimates

Given the pixel scale of 0.128"/pixel (0.06"/pixel after drizzling) and the FWHM of the PSF of  $\sim 0.2''$ , the WFC3

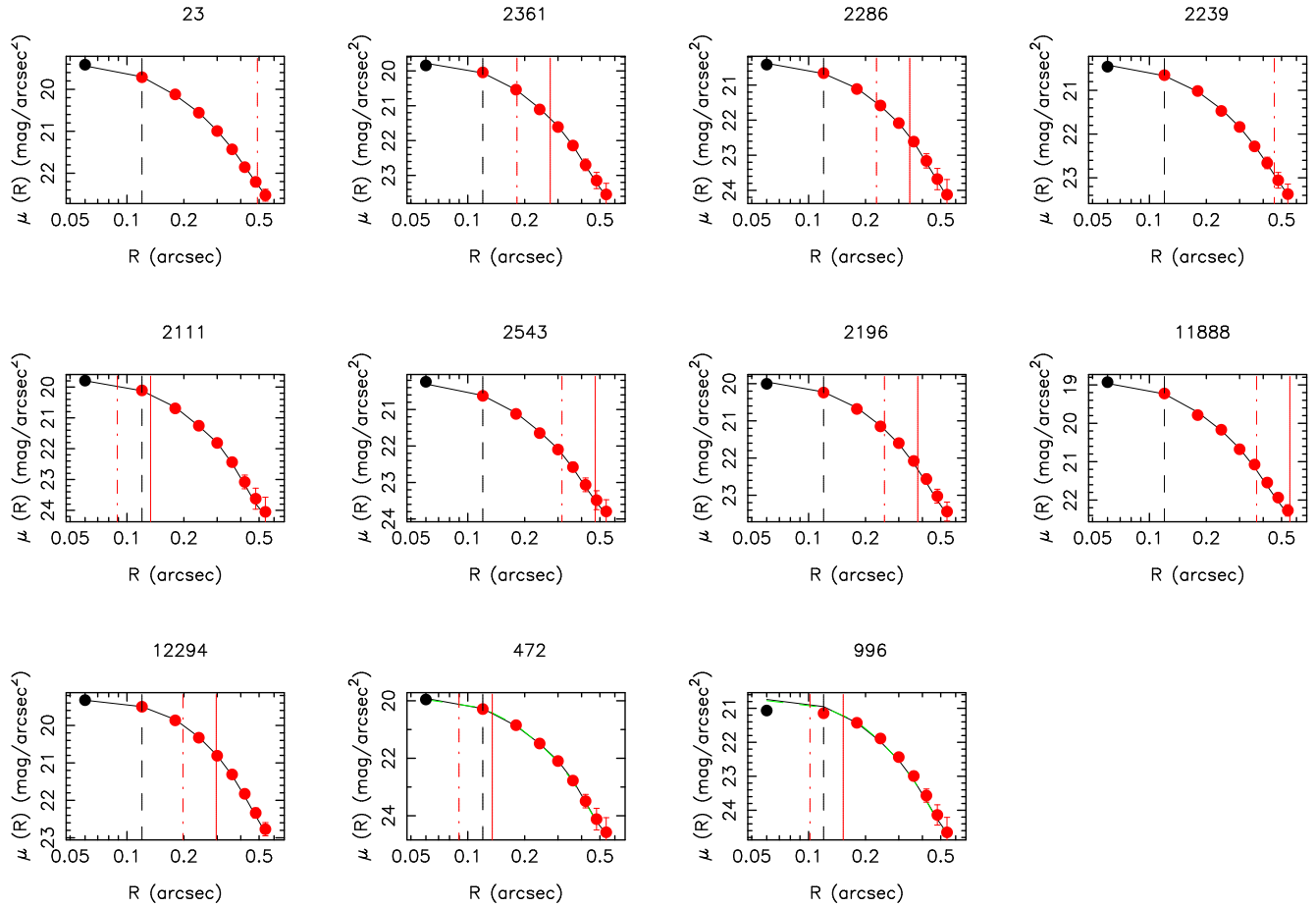


**Figure 2.** Comparison of F160W PSF-convolved Sersic profiles (black curves) for our sample of 11 ETGs, with the observed surface brightness profiles measured directly on the given images (red points). Vertical dashed black lines mark the radius of the FWHM of the PSF, while red dash-dotted and solid lines correspond to 2 and 3  $r_e$ , respectively. In panels related to ETGs 472 and 996, black lines correspond to PSF-convolved Sersic profiles derived on the mosaic image of  $\sim 80$ ks, while green lines, not visible given the almost perfect overlap to the black curves, the same quantity measured on mosaic images of  $\sim 6$ ks.

**Table 1.** Our sample of galaxies. *Column 1:* id number *Column 2:* spectroscopic redshift; *Column 3:* total magnitude from GALFIT. Errors on magnitude are the formal GALFIT errors; *Column 4:* effective radius in arcsec. A typical error on the estimates of  $r_e$  is 0.02 arcsec corresponding to 0.17 kpc at  $z=1.5$ ; *Column 5:* effective radius in kpc; *Column 6:* Sersic index; *Column 7:* F850LP-F160W colour gradient. At the median redshift  $z = 1.5$  1 arcsec corresponds to  $\sim 8.5$  kpc.

Object	$z$	F160W <sub>tot</sub> mag	$r_{e,160}$ arcsec	$R_{e,160}$ kpc	$n_{160}$	$\nabla_{F850LP-F160W}$ mag/dex
23	1.04	20.80±0.01	0.2	1.98	3.47	-0.3±0.2
11888	1.04	20.44±0.01	0.18	1.50	5.39	-0.4±0.1
12294	1.21	20.93±0.01	0.10	0.82	2.18	-0.72±0.05
996	1.39	22.57±0.01	0.05	0.43	5.52	-1.0±0.1
2239	1.41	21.74±0.01	0.23	0.38	2.85	-0.5±0.3
2286	1.60	22.20±0.01	0.11	0.97	2.02	-0.1±0.2
2361	1.61	21.60±0.01	0.09	0.77	3.35	-0.1±0.1
2196	1.61	21.65±0.01	0.12	1.06	2.81	-0.2±0.2
2543	1.61	21.93±0.02	0.15	1.33	5.62	-0.8±0.4
2111	1.61	21.85±0.01	0.04	0.38	4.73	-0.54±0.07
472	1.92	22.12±0.01	0.04	0.38	3.23	-0.6±0.1

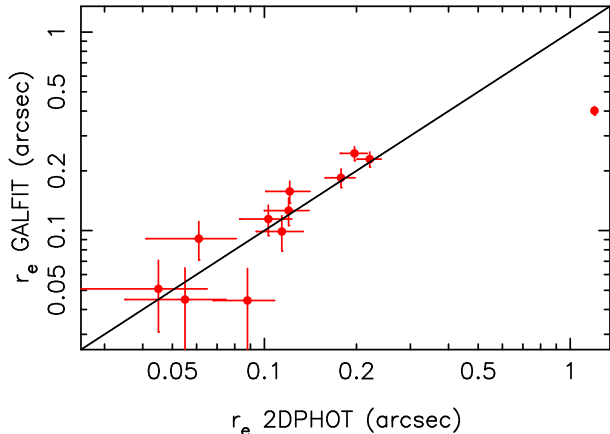


**Figure 1.** Comparison of effective radius estimated with GALFIT and 2DPHOT (see the text). The solid line marks the one-to-one relation.

images in the F160W passband are close to the sampling limit. Moreover, even with the excellent spatial resolution of WFC3, most of the high- $z$  ETGs in our sample have sizes comparable to the FWHM. This makes of paramount importance the accuracy and reliability of the derived PSF used to convolve the galaxy model. To assess the independence of our results from the method we have adopted to derive the PSF and the consequent robustness of the derived structural parameters, we have derived them also with 2DPHOT (La Barbera et al. 2008), a software working by means of different approach than GALFIT. 2DPHOT is a fully automatic tool, allowing galaxy surface photometry to be performed by fitting galaxy images with two-dimensional, PSF convolved, (Sersic) models. Differently from GALFIT, 2DPHOT constructs a PSF model in a user-independent manner, fitting star images on a given frame with a combination of two-dimensional Moffat functions, taking into account PSF asymmetries and image (under-)sampling<sup>1</sup>. In order to reproduce the spikes of the HST PSF, we have modified the 2DPHOT PSF fitting algorithm by smoothing the (average) residual map from the fitted stars (with a 3x3 pixels median smoothing), and adding the smoothed residuals to the Moffat-based PSF. The 2DPHOT initial parameters for Sersic fitting are also computed through a user-independent approach (in contrast to GALFIT), by comparing the galaxy image with a discrete grid of PSF-convolved Sersic models, reducing the problem of spurious convergences in the (non-linear) optimization procedure. In general, we find a very good agreement between 2DPHOT and GALFIT structural parameters. As an example, in Fig 1, we compare the effective radii derived with the two softwares. Errors in  $r_e$  has been set equal to 0.02 arcsec, the typical uncertainty of this measure as we have derived through monte-carlo simulations (e.g. Longhetti et al. 2007). No systematic difference is found between  $r_{e,GALFIT}$  and  $r_{e,2DPHOT}$ , despite of the different approach and methodology adopted. Only for one galaxy, with  $r_{e,GALFIT} \sim 0.4''$ , the  $r_e$  estimate

<sup>1</sup> To this effect, at each step of the PSF fitting, the Moffat functions are convolved with a box kernel, i.e. the pixel of the given image.

differs significantly, with  $r_{e,2DPHOT}$  being  $\sim 3$  times larger than  $r_{e,GALFIT}$ . Given this discrepancy, we have excluded this object from our sample thus leaving with 11 galaxies in our analysis (see Sec. 2). To be consistent with GSL11, where we estimated structural parameters in the F850LP and F606W passbands with GALFIT, we have decided to adopt GALFIT estimates of surface brightness parameters also for the WFC3/F160W filter.

To further verify the reliability of surface brightness parameters, in Fig. 2 we compare the best-fitting PSF-convolved Sersic profiles (black curves), with the observed surface brightness profiles (red points), measured in concentric circular coronas of fixed width on the F160W images. Errors on surface brightness were derived with SEXTRACTOR (Bertin & Arnouts 1996) and take into account the correlated noise introduced by the drizzling technique (Casertano et al. 2000). The vertical dashed black lines mark the radius of the FWHM of the PSF (0.1 arcsec), while red dash-dotted and continuous lines correspond to 2 and 3  $r_e$ , respectively. The figure shows an excellent agreement between observed and fitted profiles, from the very central region out to a radius of  $\sim 3r_e$ , and in many cases well beyond, both for galaxies in the deepest images (ID 472, 996) and those in the shallowest fields. This confirms the accuracy of PSF modeling and Sersic fitting. For the two galaxies on the HUDF area (ID 472 and 996), the green lines show the PSF-convolved Sersic profiles estimated on a mosaic image created to match the exposure time of the shallowest images available ( $\sim 6$  ks; see Sec. 2). The excellent agreement between the black ( $\sim 80$  ks) and green ( $\sim 6$  ks) solid curves (in fact overlapping) in the Figure indicates the homogeneity of our measures and proves the feasibility of deriving reliable structural parameters even with 2-orbit-long images. In Table 1 we report our effective radii,  $r_e$  (in units of arcsec), and  $R_e$  (in kpc), as well as the Sersic index and total magnitude for each of the 11 ETGs in our sample.

#### 4 F850LP-F160W COLOR GRADIENTS OF HIGH-Z ETGS

We recall that color gradients are generally defined as the logarithmic slope of the color profile:

$$\nabla_{F850LP-F160W} = \frac{\Delta(\mu_{F850LP} - \mu_{F160W})(R)}{\Delta \log R}. \quad (2)$$

To obtain the measure of this quantity, we have re-estimated the surface brightness parameters in the F850LP band, keeping fixed in the fit of each galaxy the ellipticity and position angle to the values derived for the F160W filter. This ensures that both the  $\mu_{F850LP}(r)$  and  $\mu_{F160W}(r)$  profiles trace the variation of light density in the same radial direction. Following the prescription commonly adopted for nearby ETGs and for consistency with GSL11, we have fitted the slope of the color profile between  $0.1r_{e,F850LP}$  and  $1r_{e,F850LP}$ . The best-fitting line is obtained by an orthogonal least-squares fit, less sensitive to outliers than the direct fit. Fig. 3 reports the results. Black curves indicates the color profiles, while red lines are the fitted slopes. Dashed lines mark the radius of the FWHM of the PSF, while colored area set  $1\sigma$  errors.

The values of the gradients and their relative errors are reported in Table 1. The error on color gradients is an upper

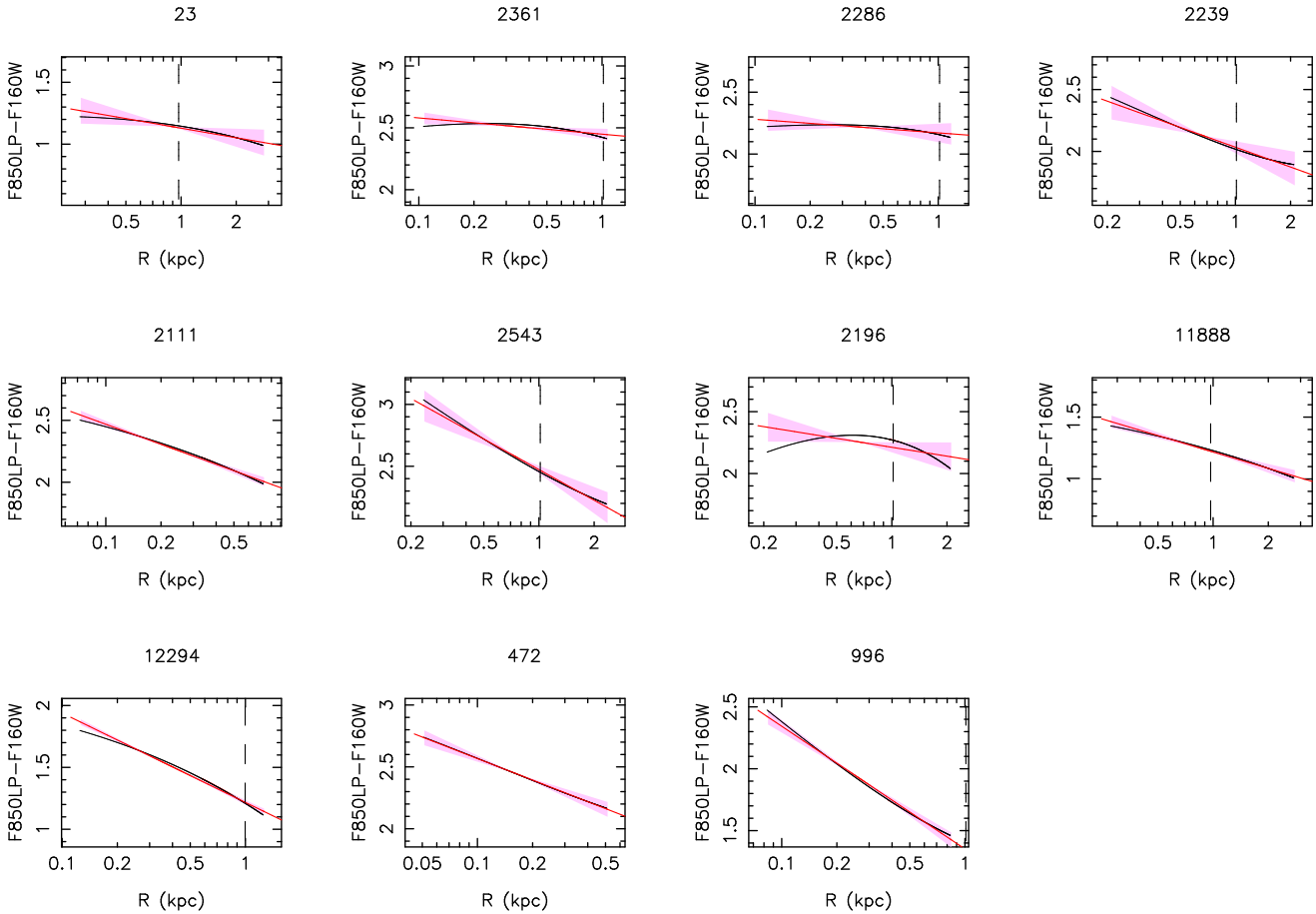


**Figure 3.** The colour gradients for the galaxies of our sample. Black lines represent the deconvolved colour profiles between  $0.1R_e$  and  $R_e$ , and the red lines are the best fitted lines to the models. The dashed vertical lines correspond to the radius of the FWHM of the PSF. Colored area indicate the  $1\sigma$  errors on colour profile slopes.

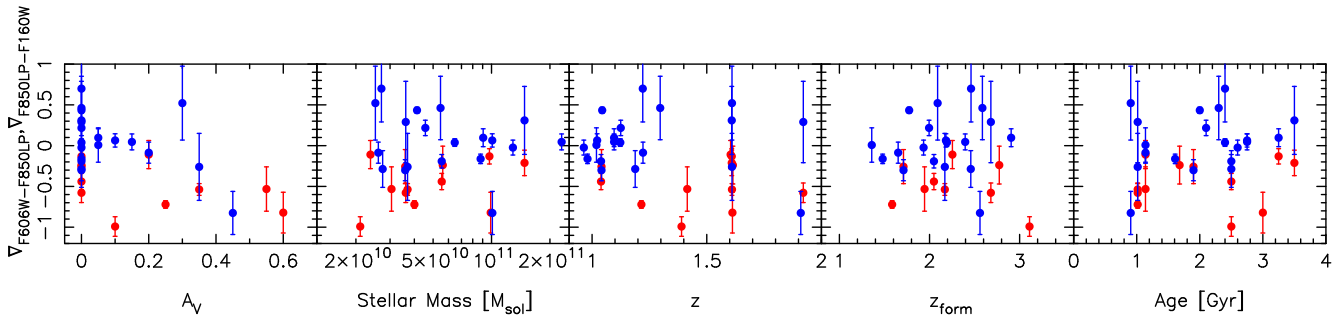


**Figure 4.** The colour gradients F606W-F850LP and F850LP-F160W (blue and red points, respectively) versus, from left to right, the dust extinction  $A_V$ , the stellar mass, the redshift, the formation redshift and the global age.

limit to the true error. We estimated it by associating, at each point of the color profile, the error on color,  $\delta col$ , measured directly from the real images in a thin circular corona of radius  $r_e$  (for galaxies with  $r_e > \text{FWHM}/2$ ), or  $\text{FWHM}/2$  (for galaxies with  $r_e < \text{FWHM}/2$ ). The  $\delta col$  was estimated after reporting the F160W and F850LP images to the same pixel scale and PSF (see Sec. 5.1). Our results show that the high- $z$  ETGs in our sample have negative or null F850LP-F160W color gradients. Indeed, 3 galaxies have color gradients comparable at  $1\sigma$  with zero. On the contrary, the remaining galaxies show significant negative values which

reveal the presence of stellar populations redder in the center than those at  $1R_e$ . The differences observed in the radial variation of the F850LP-F160W color within the galaxies of our sample show that after 3-4 Gyr at maximum from their birth, the stellar content distribution of high- $z$  ETGs was not homogeneous. This non homogeneous distribution of the stellar content within the galaxies of our sample corroborates the idea that ETGs have assembled their mass through different mechanisms.

To gain insight into the origin of the observed distribution, we firstly have looked for the presence of any cor-

relation of observed color gradients with global properties of ETGs. Fig. 4 reports the F606W-F850LP (blue points) and F850LP-F160W (red points) color gradients versus the dust extinction  $A_V$  (first panel), the total stellar mass (second panel), the redshift (third panel), the formation redshift (fourth panel; see Saracco et al. (2011) for the definition and estimate of formation redshift) and global age (last panel) of the galaxy. No correlation was detected. Indeed, the absence of a correlation could be due to the fact that we plot color variation within  $1R_e$  versus quantities estimated on the entire galaxy. We have verified that the result does not change when the color gradients are estimated throughout the whole galaxy. Thus, the various mechanisms responsible of the different stellar content observed in our high- $z$  ETGs, at the extend of our sample, produce color gradients which are independent from redshift, formation redshift, stellar mass, global age and dust extinction. This result confirms that the observed distribution of color gradients is primarily due to differences in the stellar content of high- $z$  ETGs. Different results were reached by Guo et al. (2011) who found a correlation between dust and color gradients in the direction of steeper gradient for galaxies with higher dust-obscuration. Guo et al. (2011) fixed the dust extinction assuming a Salpeter IMF in the SED fitting, while we have adopted a Chabrier IMF. Furthermore they derived their color gradients fitting the color profiles between  $\sim 1r_e$  up to  $5-8r_e$ . To properly compare our results with those of Guo et al., we have re-estimated the color gradients in our sample in regions similar to those selected in their paper, and computed  $A_V$  assuming a Salpeter IMF (see Table 2). Even in this case we do not find any correlation between dust extinction and color gradients. Actually, two galaxies of our sample were analyzed also in Guo’s paper (ID 472 and 996 our paper, 23555 and 22704 in their). Our estimates of the effective radius of these two galaxies are  $\sim 13\%$  smaller than their ones, thus consistent within the typical errors on this quantity. Moreover, for both galaxies our estimates of  $A_V$  are consistent with those reported by Guo et al. (2011). Since Guo et al. (2011) did not report the gradients values, we try to qualitatively compare our color profiles with their ones. We would like to stress here that, for these galaxies, the typical error on color at  $7r_e$  is  $\sim 0.15$  mag. For the galaxy 472 (see our Fig.7 and magenta line in the lower panel of their fig. 5) the agreement between the two color profiles seems very good. For the galaxy 996 we have found a global negative trend in color values, but the amplitude of the color gradient we detect is less steep than the one measured by Guo, due to the external region ( $5r_e < r < 7r_e$ ) where their profile falls suddenly down, while our one follows a quite constant variation (see our Fig.7 and green line in the lower panel of their fig. 5). The reason for this difference can be due to the presence of another galaxy at very low projected distance (see our Section 5.1 and their Fig. 1). In the F850LP band, this source is not detected due to its faint magnitude, thus the extreme blue color observed in the external region by Guo et al. could be due to an underestimate of the flux in the solely F160W band. On the contrary, in the fitting procedure of the surface brightness profile, we have simultaneously modeled both galaxies and assured from the residual map that the contribution of the other galaxy was properly taken into account. If this explanation is correct, the consequent flattening of the color gradient value of this

galaxy would strongly weaken the correlation between color gradients and extinction also in their sample and the eventual residual correlation should be totally due to the small statistics of their sample.

## 5 SPATIAL DISTRIBUTION OF STELLAR POPULATIONS IN HIGH-Z ETGS AND RADIAL VARIATION OF THEIR PROPERTIES.

In order to constrain the possible physical mechanisms responsible of the mass accretion within the ETGs, we have designed a new method able to investigate the spatial distribution of the underlying stellar populations in high- $z$  ETGs which is directly correlated to the mass assembly processes. Briefly, we have derived the color maps of our galaxies and, on their basis, we have defined for each ETG of our sample an internal and an external region. Then, we have modelled the *global* stellar content of each ETG as formed by two main stellar components, one dominating the internal regions, and the other the external ones. With synthetic models of composite stellar populations we have constrained the stellar properties of the two components in order to simultaneously reproduce the observed color gradient(s) (in one or two colors) and the whole global SED of the galaxy from  $0.3\mu\text{m}$  to  $8\mu\text{m}$ .

### 5.1 Color maps of high- $z$ ETGs: a direct look at the spatial distribution of their stellar content.

To have a direct look on the punctual 2-dimensional distribution of F850LP-F160W color in high- $z$  ETGs, we have derived their color maps. To this aim, we have re-reduced the WFC3 images to a pixel scale of  $0.03$  “/px to match the one of F850LP-mosaic images, and used the IRAF tasks geomap/geotran to align the two mosaics. Then, we have degraded the F850LP images (FWHM  $\sim 0.12''$ ) to the same PSF of the F160W images (FWHM  $\sim 0.2''$ ). To this aim, we needed to derive the kernel function  $K(r)$  which regulates the transformation between the PSFs in the two bands, i.e. which holds:

$$PSF_{F850LP}(r) \star K(r) = PSF_{F160W}(r) \quad (3)$$

where  $PSF_{F850LP}(r)$  and  $PSF_{F160W}(r)$  are the point spread functions in the F850LP and F160W band, respectively, and where the symbol  $\star$  denotes a convolution. For each galaxy, we have modeled its  $PSF_{F850LP}(r)$  and  $PSF_{F160W}(r)$  functions and through Eq.3 we have recovered its kernel function. The  $PSF_{F850LP}(r)$  and  $PSF_{F160W}(r)$  functions of a given galaxy have been derived by fitting the light profiles of the unsaturated stars we have adopted as PSF in GALFIT and that we have already tested to be a good approximation of the *true* PSF for that galaxy. In Figure 5 we report a representative example of the fractional encircled energy for the real PSF (black line) of a star in the F160W (left panel) and F850LP (central panel) band and the corresponding fitted model (red line). The agreement between the two curves is extremely good in both cases, confirming the quality of our fit. In the last panel of Fig. 5 we report the encircled energy distribution of the  $PSF_{F160W}(r)$  (black line) and of the



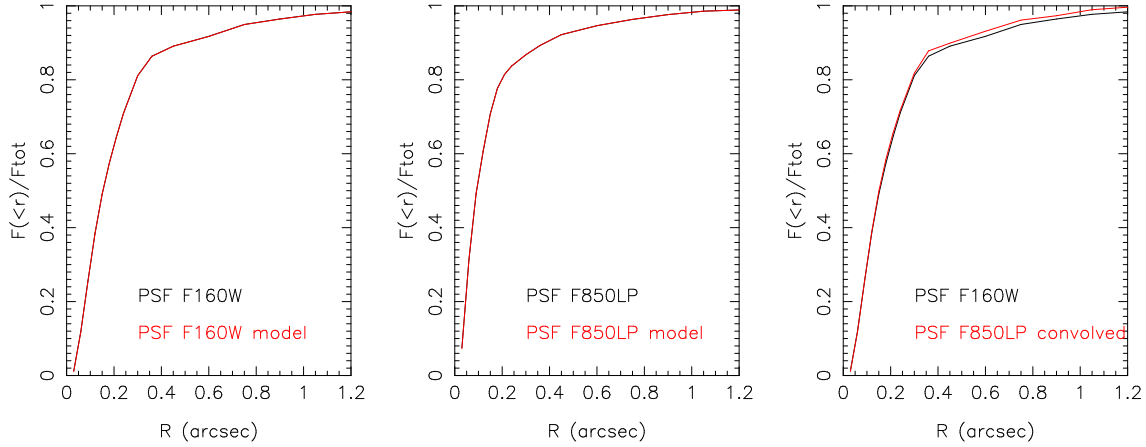


**Figure 5.** *Left panel:* the fractional encircled energy for the real PSF in the F160W image (black line) and for the model (red line). *Central panel:* the same for the F850LP image. *Right panel:* the fractional encircled energy for the real PSF in the F160W image and for the PSF of the F850LP image convolved with the kernel function  $K(r)$ .

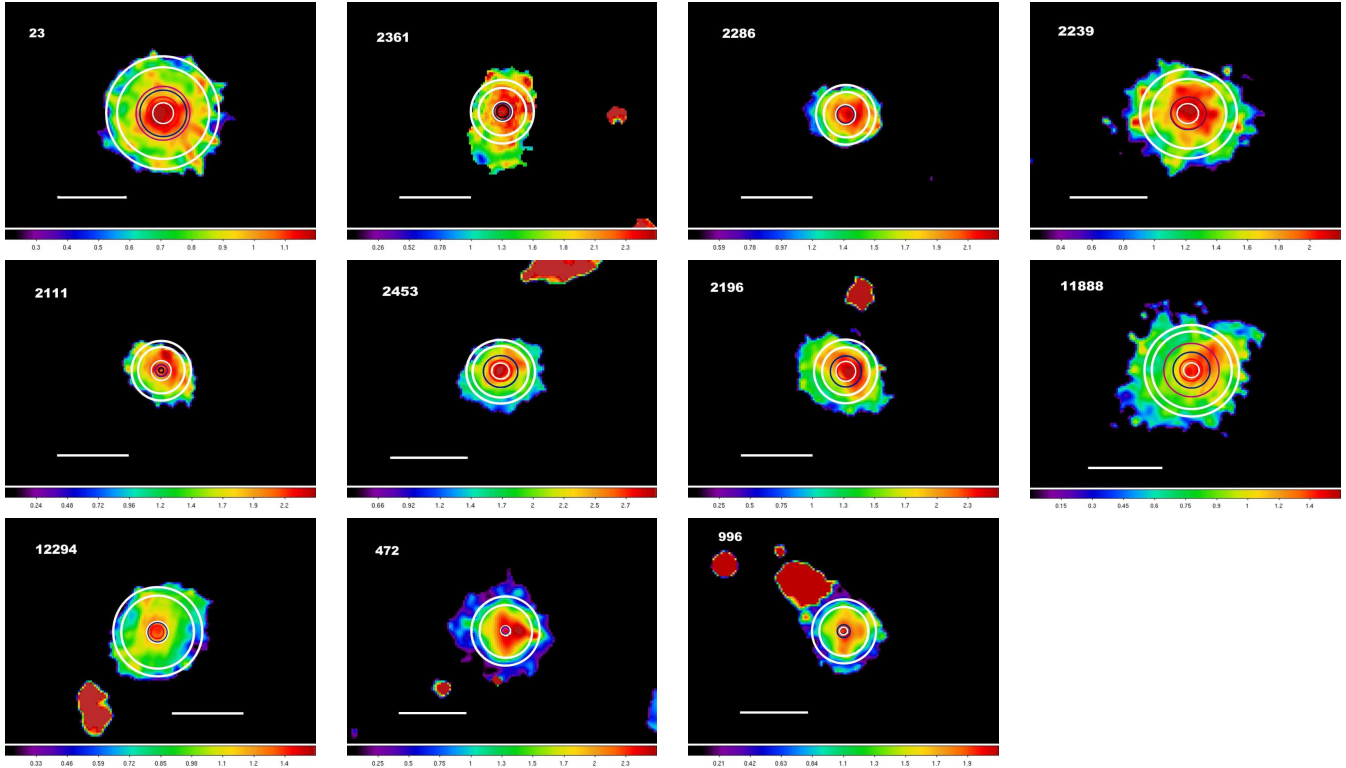


**Figure 6.** F850LP-F160W colour maps for the galaxies of our sample. The maps are color coded, indicating, from blue to red, region of the galaxy characterized by a redder emission. For each galaxy, the inner white circle constrain the internal region, while the two external ones define the circular corona which identify the external region. Magenta, blue and red circles set the effective radius in the F606W (when available), F850LP and F160W band, respectively. The white line corresponds to 1 arcsec.

$\text{PSF}_{F850LP}(r)$  model convolved with the kernel (red line). The match between the two functions is perfect and differences  $< 2\%$  appear at  $R > 4''$ , when present. In particular, it is to note the optimal agreement in the central region that, as said before, is the one mainly affecting the galaxy light profile. This has allowed us to degrade the F850LP images to the same PSF of F160W images and to derive the color maps presented in Fig. 6. The images are color coded with the reddest color indicating the region of the galaxies

with highest F850LP-F160W values. Red, blue and magenta circles indicate the  $r_e$  in the F160W, F850LP and F606W band, respectively. As pointed out before, we have at disposal information on F606W band only in 4 galaxies out of 11. In some cases the  $r_e$  in the F160W band is represented with a black circle being the red one not visible on the color map. The white lines correspond to 1 arcsec. In Fig. 6 we have marked all the pixels  $4.5\sigma$  above the mean background in the F160W images as belonging to the galaxy. In spite of



this high threshold, the color maps extend to regions well beyond  $2r_{e,F850LP}$  and at radius greater than  $4r_{e,F850LP}$  for 5 cases (12294, 996, 2361, 2111, 472). The color map of the whole galaxy show that differently from the gradients estimated up to  $1r_{e,F850LP}$ , all high- $z$  ETGs of our sample have a negative color gradient. Moreover, they point out that although the general trend is the same, the F850LP-F160W color varies from the internal to the external regions with different gradients showing that both the spatial distribution and the properties of the stellar content are not homogeneous in high- $z$  ETGs.

## 5.2 Radial variation of the stellar populations properties of high- $z$ ETGs.

To identify the stellar population parameters whose variation can account for the observed color gradients, we have used the following procedure. On the basis of the color maps which show a quite radial variation of color within the ETGs of our sample, we have schematized the whole stellar content of each of them with a two-components model assuming that a component dominates the central regions and the other dominates the external regions. By means of the color maps we have selected the two areas (white circles in Fig. 6) in order to maximize both the difference in the mean color of the two regions and the radial distance among them. At fixed gradient, maximizing the distance of the two regions means maximizing their color difference, and this will facilitate in detecting differences between the stellar population parameters of the two components and hence in detecting possible radial variations.

We have assumed as initial guess for the stellar parameters of the two components the values derived from the fit of the global SED [ $Age_{global}$ ,  $Z_{global}$ ,  $A_{V,global}$ ,  $\tau_{global}$ ]. Briefly, for each galaxy, the global stellar population parameters were derived through the fit of the spectral energy distribution defined by 14 photometric points and with known spectroscopic redshift. The fit was performed with the software Hyperzmass (Bolzonella et al. 2000) using the composite stellar population models of Charlot & Bruzual (hereafter CB07) with an exponentially declining star-formation history ( $\propto \exp^{-t/\tau}$ ), and a Chabrier initial mass function (Chabrier 2003). The best solution was selected on a grid of model with varying age, star-formation time scale  $\tau$  [0.1, 0.3, 0.4, 0.6] Gyr, and solar metallicity. Extinction  $A_V$  was left as free parameter in the 0.0 - 0.6 range and extinction curve of Calzetti et al. (2000) was adopted. For more details on SED fitting see Saracco et al. (2010). For each galaxy of our sample, the set of the four best-fit parameters are reported in Table 2.

In order to reproduce the color gradient we observe, it is necessary that one or more parameters of the two components vary from the internal to the external region. Unfortunately, the effect of age, metallicity, dust and  $\tau$  variation on the galaxy emission is degenerate in the spectral region we are observing, preventing, in fact, to identify the contribution of each parameter to the total emission. For this reason, we have performed our analysis by investigating the effect of each single parameter in turn, without considering the possibility of either a correlated or an anticorrelated variation of age and metallicity within galaxies. Thus, we have fixed in both components three out of the four parameters in the

fitting. For example to investigate radial age variation as possible driver of color variations, we fixed the metallicity, the dust extinction and the star-formation time scale to the value obtained by the fit of the global SED:  $Z_{global}$ ,  $A_{V,global}$ ,  $\tau_{global}$ . We have looked for the value of age to be associated to the internal and to the external populations,  $Age_{in}$  and  $Age_{out}$  respectively, which best reproduce the observed color gradients. In particular we have chosen the value of  $Age_{in}$  so that minimizes the quantity

$$|(F850LP - F160W)_{mod,in} - (F850LP - F160W)_{obs,in}| + |(F606W - F850LP)_{mod,in} - (F606W - F850LP)_{obs,in}| \quad (4)$$

where  $(F850LP-F160W)_{mod,in}$  and  $(F606W-F850LP)_{mod,in}$  are the F850LP-F160W and the F606W-F850LP colors predicted by the model defined by the stellar population parameters ( $Age_{in}$ ,  $Z_{global}$ ,  $A_{V,global}$ ,  $\tau_{global}$ ), and  $(F850LP-F160W)_{obs,in}$  and  $(F606W-F850LP)_{obs,in}$  are the mean value of the colors observed in the internal region. Similar procedure has been adopted to identify  $Age_{out}$ . In the cases for which F606W-F850LP color gradients are not available we clearly ignore the second lines in Eq.4. To fix the contribution to the total stellar mass of the two components so selected, we fit the global SED sampled by 14 photometric points with a linear combination of the SEDs of the two populations.

We have repeated this analysis also for variation of metallicity  $Z$ , keeping fixed [ $Age_{global}$ ,  $A_{V,global}$ ,  $\tau_{global}$ ], and star-formation  $\tau$  with [ $Age_{global}$ ,  $Z_{global}$ ,  $A_{V,global}$ ] fixed. We have looked for the values of metallicity to be associated to the internal and external population,  $Z_{in}$  and  $Z_{out}$  respectively, on a grid of sub-solar and super-solar values:  $0.2Z_{\odot}$ ,  $0.4Z_{\odot}$ ,  $Z_{\odot}$  and  $2Z_{\odot}$ , while for the star-formation time scale we have considered the range 0.1 -0.6Gyr.

### 5.2.1 An example

In Fig. 7 we report an example of the analysis described above for a galaxy of our sample. We select a case which presents some peculiarities to guide the interpretation of the analysis in this more complex case and left to the reader the interpretation of the analysis of the other galaxies not discussed here but presented in electronic form. The first column reports the analysis relative to the effect on galaxy colors of pure age variation from the inner to the outer regions. The second and the third column show the same but for metallicity and  $\tau$  radial variation, respectively. In each column we report, from top to bottom, the F850LP-F160W color gradient, the F606W-F850LP color gradient, when available, and the global SED. In the panels related to the color gradients, the black lines are the color profiles. Red lines are the fit to the color profiles up to the external regions derived following the same method describe in Section 4. Red points are the mean color values of the internal regions measured through color profiles, i.e.  $(F850LP-F160W)_{obs,in}$  and  $(F606W-F850LP)_{obs,in}$  in Eq. 4. Blue points are the same for the external regions. The horizontal error bars indicate the extension of the two areas we select (white circles in color maps) and over which we computed the mean colors.

In the bottom panel we report the observed SED (black dots), the best fitting template (black line) and the relative

**Table 2.** Stellar population parameters derived from the fit of global the SED assuming a Chabrier IMF and a Salpeter IMF. *Column 1:* id number; *Column 2:* Age obtained with a Chabrier IMF|Age obtained with a Salpeter IMF; *Column 3:*  $\tau$  obtained with a Chabrier IMF| $\tau$  obtained with a Salpeter IMF; *Column 4:*  $A_V$  obtained with a Chabrier IMF| $A_V$  obtained with a Salpeter IMF; *Column 5:*  $\log M_\star$  obtained with a Chabrier IMF| $\log M_\star$  obtained with a Salpeter IMF. In each fit we assume solar metallicity.

Object	Age <sub>Cha</sub>  Age <sub>Sal</sub> Gyr	$\tau_{Cha}$   $\tau_{Sal}$ Gyr	$A_{V,Cha}$   $A_{V,Sal}$ mag	$\log M_{\star,Cha}$   $\log M_{\star,Sal}$ $M_\odot$
23	1.90 2.1	0.1 0.1	0.0 0.0	10.5 10.9
11888	2.5 2.4	0.3 0.3	0.0 0.0	10.7 11.0
12294	1.0 1.0	0.1 0.1	0.25 0.25	10.6 10.9
996	2.5 1.7	0.3 0.2	0.10 0.30	10.3 10.5
2239	1.1 1.1	0.1 0.1	0.55 0.60	10.5 10.8
2286	1.1 1.1	0.1 0.1	0.20 0.25	10.4 10.7
2361	3.25 3.25	0.3 0.3	0.0 0.0	11.0 11.3
2148	3.5 3.25	0.4 0.4	0.0 0.05	11.2 11.4
2196	1.7 1.9	0.1 0.2	0.0 0.05	10.7 11.10
2543	3.0 3.25	0.4 0.5	0.6 0.6	11.0 11.3
2111	1.0 1.0	0.1 0.1	0.35 0.60	10.6 11.3
472	1.0 1.0	0.1 0.1	0.0 0.0	10.6 10.9

best fitting parameters (black text). Red and blue lines are the contribution of the internal and external population, respectively, to the total emission, and hence to the total stellar mass. The amount of their contribution was fixed such that their linear combination (magenta, cyan or green lines for age, metallicity and  $\tau$  variations, respectively) minimizes the residual with the observed SED. In each panel we report the  $\chi^2$  value of this fit. In red we present the value of the varying parameter which minimize the Eq.4 as well as their contribute in mass, and in blue the same for the external region.

The solely linear radial variation of this parameter from the internal value (red text), to the external value (blue text) will produce a F850LP-F160W and a F606W-F850LP color gradient indicated in the top and middle panels by the dashed lines (magenta, cyan and green in the case of age, metallicity and  $\tau$  variation) Fig. 7 shows that the color gradient we observe in this galaxy can be due to a variation of the age of the stellar populations from the inner to the outer regions. Indeed, while the global fit returns us a mean age of 1.9 Gyr (black text in the bottom left panel), our analysis shows that a population of 2.7 Gyr dominating the central region (red text in the bottom left panel) and a younger population of 1.0 Gyr dominating the external regions (blue text in the bottom left panel), can perfectly reproduce within the errors (magenta dashed line in top and middle panels) the internal and external observed F606W-F850LP and F850LP-F160W colors, and hence the color gradients. Further, the analysis of the SED suggests that in this galaxy the older stellar population contributes to the stellar mass for more than 90% (red line, bottom left panel). On the contrary, neither a pure metallicity variation, nor a variation of the star-formation time scale alone can reproduce the observed color gradients. In the case of metallicity (middle column), the internal colors are well reproduced by a population with solar metallicity (red text in the bottom central panel), i.e. the same of the global fit, while the external color cannot be simultaneously reproduced by a single value of  $Z$ .

For what concerns the analysis of the  $\tau$  variation this galaxy requires particular attention. The fit of the global SED sug-

gests a mean  $\tau$  for this galaxy of 0.1Gyr, that is the lower value in the grid of the star-formation time scales considered. To cope with this, we assume a population of 2.7 Gyr with  $\tau = 0.1$  Gyr as representative of the inner part, as we already found that this parameter well fits the inner colors. For the external regions, fixing the age to 2.4 Gyr, the value of  $\tau$  that best reproduces both external colors is 0.4 Gyr. However, despite it is the best fitting value, it is not able to reproduce within  $1\sigma$  the observed F850LP-F160W external color.

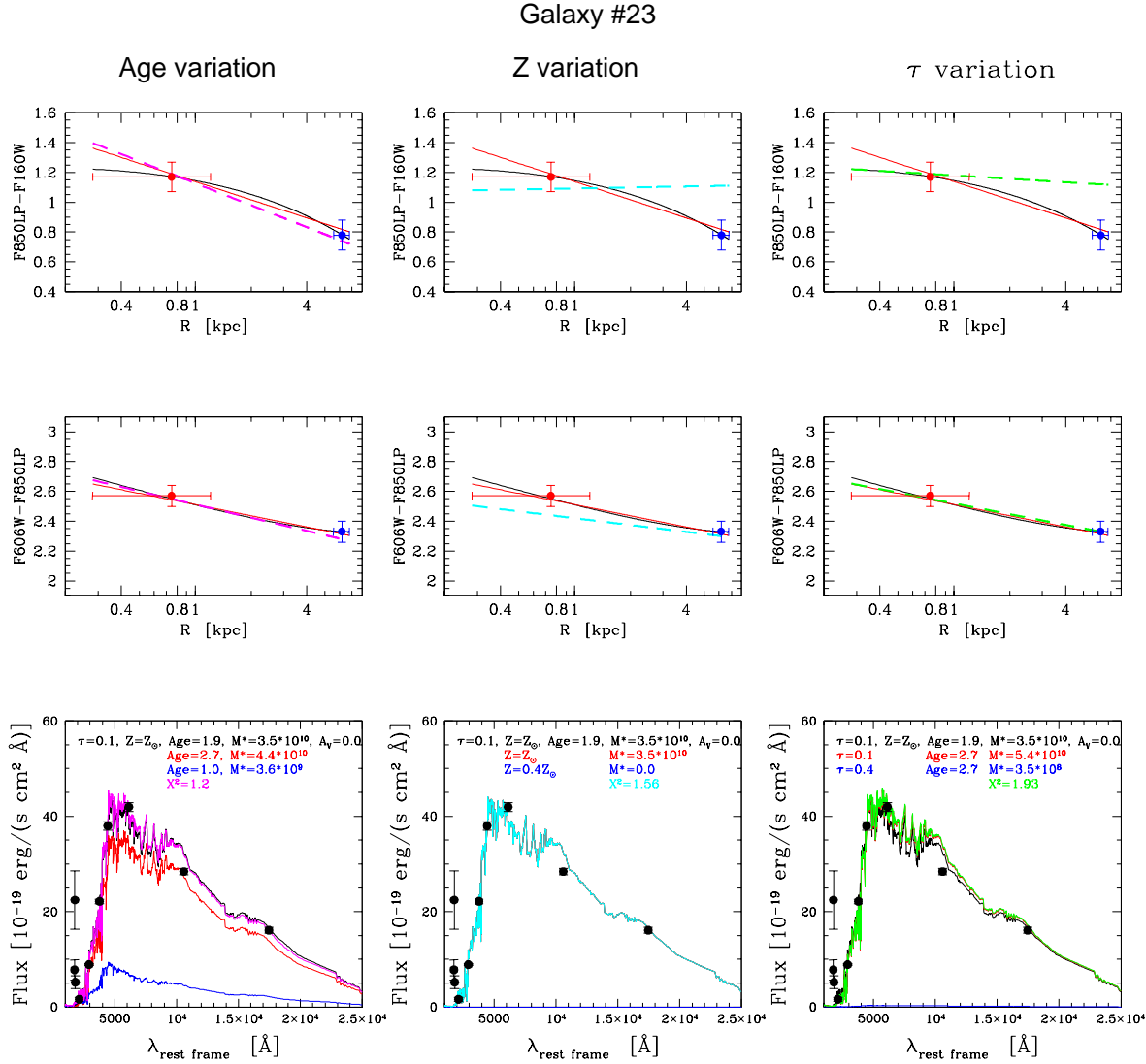


**Figure 7.** *First column:* analysis of radial age variation as possible driver of observed color gradients. Top and middle panels show the F850LP-F160W and F606W-F850LP color profiles, respectively (black lines), with the relative fit (red lines). The bottom panel shows the observed global SED (black dots) as well as the stellar population parameters (black text) derived from its fit (black line). Among all the stellar populations with varying age but star-formation time scale, metallicity and dust extinction equal to the value obtained from the fit of the global SED, the red text identifies the one that best simultaneously reproduces the colors observed in the internal region (red dots in the top and middle panel). Similarly, blue text reports the value of the age of the stellar population that best reproduce the external colors (blue dots in the upper panels). The pure linear variation of the age of the galaxy stellar populations from the internal value to the external one, will produce the F850LP-F160W and F606W-F850LP color gradients represented with the dashed magenta lines. The contribution to the total stellar mass of the two populations is fixed in order to best fit the whole SED and are reported in the bottom panel (red and blue lines). *Second and third column:* the same of first column but for metallicity and star-formation time scale variation.

**Table 3.** Color gradients produced by the variation of a single stellar population parameters from the internal to the external regions. *Column 1:* top line: galaxy id number; bottom line: compactness  $C$  defined as  $R_{e,z=0}/R_e$  where  $R_e$  is the effective radius of the galaxy and  $R_{e,z=0}$  is the radius that a galaxy of equal stellar mass would have at  $z=0$  as derived by the size mass relation of Shen et al. (2003). ETGs with effective radius more than one sigma smaller than those predicted by the local size-mass relation, turn out to have  $C \geq 2$ . ; *Column 2:* Radius up to which we extend the analysis ( $R_{ext}$ , in  $R_{e,F850LP}$  unit); *Column 3:* F850LP-F160W measured color gradient|F606W-F850LP measured color gradient derived up to  $R_{ext}$  from the fit of the color profile; *Column 4:* top line: F850LP-F160W color gradient|F606W-F850LP color gradient produced by a solely radial age variation from  $Age_{in}$  in the internal region to  $Age_{out}$  in the external region (see bottom line); bottom line:  $Age_{in}$ : age of the internal population -  $Age_{out}$ : age of the external population -  $\nabla_{age}$ : age gradient derived as  $d \log Age / d \log r$ ; *Column 5:* the same of column 4 for metallicity radial variation; metallicity gradient is derived as  $d \log Z / d \log r$ ; *Column 6:* the same of column 4 for star-formation time scale radial variation; *Column 7:* the same of column 4 for IMF's slope radial variation. In the case of star-formation time scale and IMF's slope radial variation the  $\nabla_{\tau}$  and  $\nabla_{\alpha}$  are omitted. In bold case are reported the variations able to reproduce both the color gradients and observed global SED.

ID	$R_{ext}$	$\nabla_{F850-F160,mis}   \nabla_{F606-F850,mis}$	$\nabla_{F850-F160,age}   \nabla_{F606-F850,age}$ Age <sub>in</sub> - Age <sub>out</sub> - $\nabla_{age}$	$\nabla_{F850-F160,Z}   \nabla_{F606-F850,Z}$ Z <sub>in</sub> - Z <sub>out</sub> - $\nabla_Z$	$\nabla_{F850-F160,\tau}   \nabla_{F606-F850,\tau}$ $\tau_{in}$ - $\tau_{out}$	$\nabla_{F850-F160,\alpha}   \nabla_{F606-F850,\alpha}$ $\alpha_{in}$ - $\alpha_{out}$
		mag/dex mag/dex	mag/dex mag/dex [Gyr] - [Gyr] - Gyr/dex	mag/dex mag/dex	mag/dex mag/dex [Gyr] - [Gyr]	mag/dex mag/dex
23 1.1	2.4	-0.40 -0.24	<b>-0.49 -0.29</b> <b>2.7 - 1.0 - -0.45</b>	0.02 -0.15 Z <sub>⊙</sub> - 0.4Z <sub>⊙</sub> - -0.42	-0.08 -0.24 0.1 - 0.4	-0.06 -0.05 1.5 - 3.0
11888 1.6	2.5	-0.51 -0.29	-0.19 -0.31 3.2 - 2.1 - -0.19	-0.16 -0.44 2Z <sub>⊙</sub> - 0.4Z <sub>⊙</sub> - -0.72	-0.10 -0.31 0.1 - 0.4	-0.02 -0.08 3.5 - 2.0
12294 2.3	4.5	-1.07 —	-1.27 — 1.3 - 0.3 - -0.73	-0.46 — 2Z <sub>⊙</sub> - 0.2Z <sub>⊙</sub> - -1.15	-0.81 — 0.1 - 0.6	-1.20 — 1.5 - 3.0
996 2.6	4.9	-0.59 —	<b>-0.66 —</b> <b>3.0 - 1.1 - -0.38</b>	-0.24 — Z <sub>⊙</sub> - 0.2Z <sub>⊙</sub> - -0.6	-0.34 — 0.1 - 0.6	-0.64 — 2.0 - 3.5
2239 1.3	2.8	-0.28 —	<b>-0.22 —</b> <b>1.9 - 1.1 - -0.28</b>	<b>-0.24 —</b> <b>2Z<sub>⊙</sub> - Z<sub>⊙</sub> - -0.35</b>	<b>-0.16 —</b> <b>0.1 - 0.3</b>	<b>-0.13 —</b> <b>1.5 - 3.0</b>
2286 1.9	3.2	-0.42 —	<b>-0.55 —</b> <b>1.8 - 0.8 - -0.51</b>	<b>-0.72 —</b> <b>2Z<sub>⊙</sub> - 0.2Z<sub>⊙</sub> - -1.45</b>	<b>-0.50 —</b> <b>0.1 - 0.4</b>	0.20 — 1.5 - 3.5
2361 4.4	4.3	-0.54 —	-0.51 — 3.5 - 1.8 - -0.36	-0.83 — 2Z <sub>⊙</sub> - 0.2Z <sub>⊙</sub> - -1.25	-0.30 — 0.1 - 0.6	0.06 — 1.5 - 3.0
2196 2.0	2.0	-0.70 —	<b>-0.86 —</b> <b>3.0 - 0.8 - -0.84</b>	<b>-0.82 —</b> <b>2Z<sub>⊙</sub> - 0.2Z<sub>⊙</sub> - -1.47</b>	-0.52 — 0.1 - 0.6	0.07 — 1.5 - 3.5
2543 2.6	2.0	-0.73 —	<b>-0.68 —</b> <b>3.5 - 1.8 - -0.33</b>	<b>-0.67 —</b> <b>2Z<sub>⊙</sub> - 0.2Z<sub>⊙</sub> - -1.19</b>	-0.42 — 0.1 - 0.6	<b>-0.41 —</b> <b>3.5 - 1.5</b>
2111 3.8	4.9	-0.76 0.05	0.17 0.3 1.0 - 1.1 - +0.05	0 0 Z <sub>⊙</sub> - Z <sub>⊙</sub> - 0	0 0 0.1 - 0.1	-0.01 0.02 3.0 - 3.5
472 5.4	8.6	-0.31 0.83	0.22 0.93 0.9 - 1.4 - 0.18	0.21 0.71 Z <sub>⊙</sub> - 2Z <sub>⊙</sub> - 0.28	0 0 0.1 - 0.1	-0.08 0.30 1.5 - 3.5

The fact that we have changed the global age value does not influence our analysis. Indeed, we make the starting assumption to associate to the two components the stellar population parameters of the global fit since it can be a good representation of the whole galaxy. However what we are interested in is the *variation* of these parameters as possible driver of the observed color gradients, and not their absolute values. In Table 3 we report the summary of the results obtained for the other galaxies of the sample, while the plots related to their analysis similar to Fig. 7 and with the same conventions are available in electronic form.

### 5.2.2 Dust distribution and color gradient

Actually, as pointed out before, one of the causes of the radial variation of color we observe in our ETGs can be a non homogeneous distribution of the dust within the galaxy. Fig. 4 shows that for half galaxy of our sample the fit of the global SED returns a value of  $A_V = 0$ . Thus, for these galaxies (ID 23, 11888, 2361, 2196, 472) seems not plausible a scenario whereby the main driver of the color gradients is a radial distribution of dust. For the remaining galaxies, the observed global SED was best fitted assuming the presence of a non null quantity of dust. As in the case of age, metallicity and  $\tau$  we test if, starting from a flat color distribution, a pure radial variation of the dust extinction (more dust in the center than in the outskirts) can reproduce the observed color gradients.

In particular, we have made the working hypothesis that the ETGs of the sample have no dust in the outskirts. Thus, the colors we measure in the external regions (i.e.  $(F850LP-F160W)_{obs,out}$ ) are the intrinsic colors of the galaxies. In these hypothesis, the reddest colors observed in the center of the galaxies (i.e.  $(F850LP-F160W)_{obs,in}$ ) are the direct effect of the extinction of the dust. The necessary amount of dust extinction to redden the intrinsic colors to those observed in the center is:

$$A_V = \frac{[(F850LP - F160W)_{obs,in} - (F850LP - F160W)_{obs,out}] \times R_V}{K(F850LP) - K(F160W)} \quad (5)$$

where  $K(F850LP)A_V/R_V$  and  $K(F160W)A_V/R_V$  are the extinction in both bands due to the dust. We have derived  $K(F850LP)$  and  $K(F160W)$  following Calzetti et al. (2000) and have assumed  $R_V = 4.05 \pm 0.80$ . For the galaxy 2111, Eq. 5 leads to a dust extinction  $A_V$  in the center  $\sim 1$ . This value is a lower limit. Indeed, if dust was not localized only in the center as we have assumed, but also in the periphery, the amount of dust necessary to generate the observed color gradient should be even higher. The fit of the global SED returns a global value of  $A_V = 0.35$ , much lower than the one we obtain. Moreover, the amount of dust predicted, that necessarily affects also the emission in the F606W and F850LP bands, produce F606W-F850LP color in the central region of the galaxy redder than the observed one. Thus, for this galaxy, dust does not seem the main driver of the observed color gradients.

For galaxies 2286, 2239, and 2543 the analysis indicates that, in our hypothesis, their color gradients can be obtained assuming a dust extinction in the central regions of  $A_V = 0.55$ , 0.29 and 0.83, respectively. Table 2 shows that for the galaxy 2239 the dust extinction we need to reproduce the

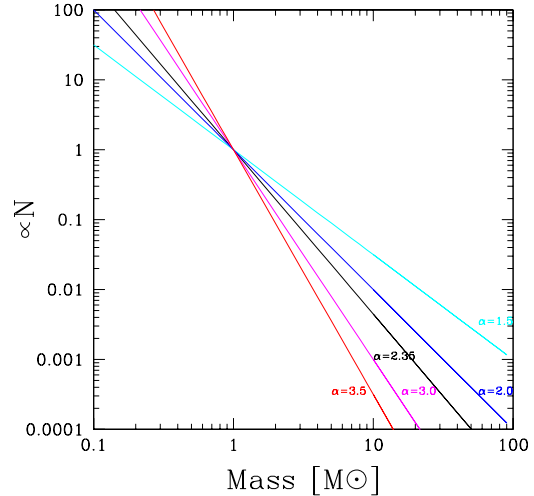


**Figure 8.** The relative amount of low-to-high mass stars predicted by 5 different IMFs with analytic form  $dN/dM \propto M^{-\alpha}$  and  $\alpha = 1.5, 2.0, 2.35, 3.0, 3.5$ .

color gradient is lower than the one predicted by the fit of the global SED. On the contrary, galaxies 2286, 2543 require a dust extinction  $\sim 1.5$ -2 times higher than the one we obtained from the global SED fitting. These values confirm that for these galaxies, if not the main driver, a significant contribution of dust in generating the observed color cannot be excluded.

Finally, for the galaxy 996 and 12294 we have obtained  $A_V = 1.08$  and 1.53 respectively, results which disagree with the best-fit values of 0.10 and 0.25. In these cases the dust extinction we need to reproduce the observed color gradients is 6-10 times higher than the one obtained from the global SED fitting, suggesting that, although it is not possible to exclude it at all, the radial variation of dust extinction is certainly not the main driver of the color variation we observe.

### 5.2.3 Radial variation of initial mass function as possible driver of color gradients

Among the main hypothesis to explain the color gradients we observe, there is also a change in the initial mass function (IMF) from the inner to the outer regions of the galaxy.

In spite of the fact that a radial variation of IMF could be a reliable way to produce color gradient, it has never been explored due to the lack of suitable stellar population models. For this reason a grid of stellar population models has been kindly produced *ad hoc* by Stephan Charlot for this purpose: reproducing the spectral energy distribution of galaxies with different proportion of low-to-high mass stars. In particular we have assumed an IMF analytically described by a power law form:

$$dN/dM \propto M^{-\alpha} \quad (6)$$

with 5 different values of  $\alpha$ : 1.5, 2.0, 2.35, 3.0, 3.5. The value 2.35 corresponds to a pure Salpeter IMF (Salpeter 1955). Fig. 8 shows the relative different amount of low-to-high mass stars produced by the 5 IMFs.

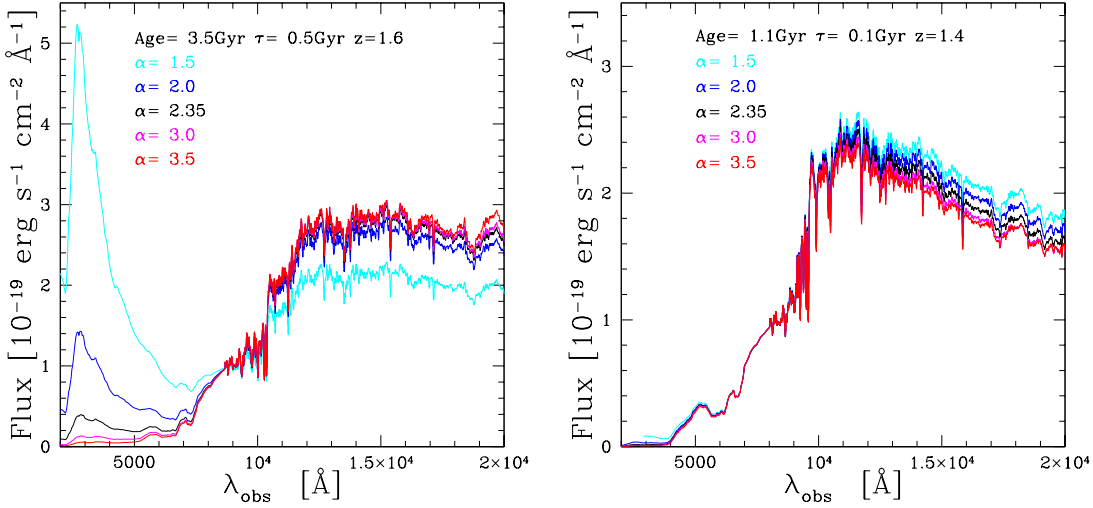


**Figure 9.** *Left Panel:* global SED of a template galaxy with Age= 3.5 Gyr and  $\tau=0.5$  Gyr at varying slope  $\alpha$  of the IMF described by the functional form  $dN/dM \propto M^{-\alpha}$ . *Right Panel:* the same of left panel but for a different ratio Age/ $\tau$ .

The evolution of a star with time is strictly related to its mass. Thus, at fixed age, metallicity, star-formation time scales, and dust extinction, the spectral energy emission of a galaxy will change with the IMF due to the different amount of low-to-high mass stars. Left panel of Fig. 9 shows how the template of the global SED of a possible galaxy of our sample (age = 3.5 Gyr,  $\tau = 0.5$  Gyr,  $z=1.6$ ) would change with different IMFs. To observe the relative differences, we have normalized the observed SEDs in the wavelength range [8250 Å- 8750 Å]. The colors of the different SED follow the same code of Fig. 8. Since we normalized all the curves approximately in correspondence of the F850LP filter, when looking at the emission around 16000 Å this plot returns immediately how the F850LP-F160W color changes with the IMF. In particular, for this template, IMF with an higher abundance of low mass stars (red line) returns redder color than the one with lower number of low-mass stars. Actually, the color of a star changes through all its life cycle, as it moves on the HR diagram according to its mass. So, the contribution of low and high mass stars to the total emission in a fixed band changes at the variation of the ratio age/ $\tau$ . Right panel of Fig. 9 shows the same plot on the left but for a galaxy with a different ratio Age/ $\tau$ . This simulated galaxy has age = 1.1 Gyr and  $\tau = 0.1$  Gyr. Even in this case, we normalize the curves in the wavelength region [8250 Å- 8750 Å]. This plot shows how in this case, the near-IR domain is dominated by the light coming from the high-mass stars contrary to the previous case. These plots clearly emphasize two main aspects: colors are affected by the IMF, hence the radial color variation we detect can be effectively due to radial variation of IMF, and the shape of the SED depends on the ratio age/ $\tau$  and IMF.

To investigate the hypothesis of an IMF radial variation as the main driver of color gradient, we have adopted the same method used to study age, metallicity and  $\tau$  radial variations. For each galaxy we have fixed the stellar population parameters of the internal and external populations to those derived from the global fit and have looked for the value of the IMF's slope able to reproduce the observed color gra-

dients. Since our goal is to investigate the radial variation of low-to-high mass stars abundance, we have re-fitted the observed global SED assuming a Salpeter IMF instead of the Chabrier. In Table 2 the result of the SED fitting with a Salpeter IMF are reported. We have assumed the internal and external populations defined by these new global parameters ( $A_{global,Sal}$ ,  $Z_{global,Sal}$ ,  $A_{V,global,Sal}$ ,  $\tau_{global,Sal}$ ,  $\alpha=2.35$ ) and we have looked for the value of  $\alpha$  to be associated to the internal and external population,  $\alpha_{in}$  and  $\alpha_{out}$  so that the two populations defined by the set of parameters ( $A_{global,Sal}$ ,  $Z_{global,Sal}$ ,  $A_{V,global,Sal}$ ,  $\tau_{global,Sal}$ ,  $\alpha_{in}$ ) and ( $A_{global,Sal}$ ,  $Z_{global,Sal}$ ,  $A_{V,global,Sal}$ ,  $\tau_{global,Sal}$ ,  $\alpha_{out}$ ) best reproduce the observed color gradients and the global SED.

In all but two cases a variation of the abundance of low-to-high mass stars can be excluded as the main driver of the observed color gradients. On the contrary Fig. 10 shows that for the galaxy 2239 an external population accounting for the great part of the mass (> 90%) formed with an IMF with  $\alpha = 3.0$ , i.e. with an higher number of low mass stars than a Salpeter, and a small contribution in mass of an internal population with an IMF defined by an  $\alpha = 1.5$  can simultaneously reproduce the F850LP-F160W observed color gradient we have derived and the observed global SED. At the same way, the F850LP-F160W color gradient and the global SED of the galaxy 2543 are well reproduced by a very massive population dominating the internal region characterized by an IMF with  $\alpha = 3.5$  and by a small contribution of an external population described by an IMF with  $\alpha = 1.5$ . As noted before, the different ratio age/ $\tau$  of these two galaxies reflects in inverted radial trend of IMF's slope to reproduce negative color gradients. Thus, for these two galaxies a variation of the slope of the IMF, and hence a variation in the abundance of low-to-high mass stars can be a possible driver of the radial color variations we detect. In Table 3, the results of the analysis for all the galaxies of the sample are shown, while in electronic form we present their plots.

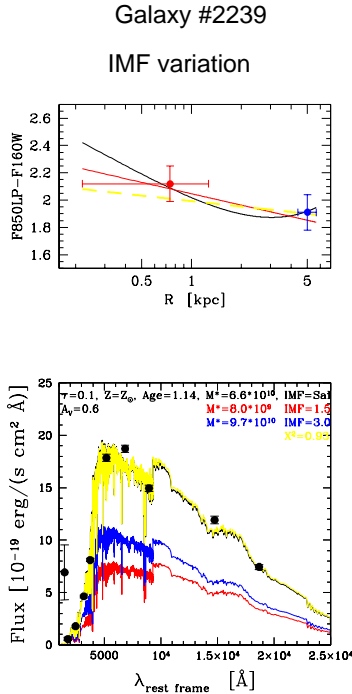


**Figure 10.** Analysis of the radial variation of IMF’s slope as possible driver of observed color gradients. Top panel shows the F850LP-F160W color profile (black line) with the relative fit (red line). The bottom panel shows the observed global SED (black dots) as well as the stellar population parameters (black text) derived from its fit (black line) assuming a Salpeter IMF. Among all the stellar populations with varying IMF’s slope but age, star-formation time scale, metallicity and dust extinction equal to the value obtained from the fit of the global SED, the red text identifies the one that best reproduces the color observed in the internal region (red dot in the top panel). Similarly, blue text reports the value of the slope of the IMF that best reproduce the external color (blue dot in the upper panel). The pure linear variation of the IMF’s slope from the internal value to the external one, will produce the F850LP-F160W color gradient represented with the dashed yellow line. The contribution to the total stellar mass of the two populations is fixed in order to best fit the whole SED and are reported in the bottom panel (red and blue lines).

## 6 SUMMARY OF THE RESULTS

We have found that  $\sim 70\%$  (8 out of 11) of the ETGs in our sample show negative color gradients at more than  $\sim 2\sigma$  ( $>4\sigma$  in 5 ETGs) in the  $0.1R_e$ - $1R_e$  range, the effective radius range usually adopted to study color gradients in local ETGs. The remaining 30% show a gradient consistent with a flat color profile. Extending the analysis at  $R > R_e$ , enclosing the whole galaxy, we have found that the fraction of high- $z$  ETGs with negative F850LP-F160W color gradients rises up to 100%. In fact, we have generally found a steepening of color gradients extending the fit to regions out of  $R_e$  ( $2R_e < R < 8R_e$ )

For 6 galaxies of our sample (ID 23, 2286, 2239, 2543, 2196, 996) a solely radial variation of the age of the stellar populations can simultaneously reproduce at less than  $1\sigma$  the observed color gradients throughout the whole galaxy and

the global SED. For four of these galaxies (ID 2286, 2239, 2196, 2543), also radial metallicity variation can reproduce the color gradient. On the contrary, a radial variation of the star-formation time scale, dust content, and abundance of low-to-high mass stars are able to reproduce both color gradients and global SED in only few of these 6 galaxies. Moreover, we pointed out that a radial variation of the slope of the IMF is not able to reproduce the observed radial color variation and spectral emission in any of the four galaxies for which both F606W-F850LP and F850LP-F160W color gradients are available.

These results assign to age and metallicity a central role in generating the observed color gradients. As pointed out before, a contribution of other parameters to the color variations we detected cannot be ruled out.

For the remaining five galaxies (ID 2111, 11888, 12294, 472, 2361) the variation of a single stellar population parameter is not able to reproduce the observed color gradients and global SED consistently with the findings of Guo et al. (2011) on their sample. This suggests that for these galaxies a simultaneous variation of several parameters has to be invoked to reproduce the observed color variations and global SED. For these galaxies, an approach that investigates the simultaneous variation of more than one parameter should be considered.

## 7 DISCUSSION AND CONCLUSIONS

The results of our analysis establish the heterogeneity of the stellar content in high- $z$  ETGs. For  $\sim 50\%$  of the galaxies of our sample (6 ETGs) we have found that a pure radial age variation, with the oldest stars located at the center of the galaxy, is able to reproduce the observed radial color profile and global SED. The age gradients we have detected for these galaxies span a range from  $-0.84$  to  $-0.28$  dex per radial decade. For 4 out of these 6 ETGs the color gradients we have observed can be also accounted for by solely metallicity gradients whose strength varies from  $-0.35$  to  $-1.45$  dex per radial decade.

Due to the lack of similar measurements on other sample of high- $z$  ETGs we have compared the age/metallicity gradient values we have found with those observed in the local ETGs. Studies of ETGs at lower redshift affirm that color gradients are mainly due to radial metallicity variations. Assuming the age of the stellar populations constant throughout the galaxy, as we did in the case of metallicity gradient analysis, color gradients in local ETGs turn out to be reproduced by a mean metallicity gradients ranging from  $-0.16$  to  $-0.3$  (Peletier et al. 1990; Idiart et al. 2003; Tamura & Ohta 2003). A further confirmation of the metallicity as main driver of local gradients comes out from studies at intermediate redshift which show that the color gradients evolution is better accounted for by the passive evolution of metallicity gradients (Saglia et al. 2000; Hinkley & Im 2001). In fact, our results seem to be inconsistent with these findings. In our sample of high- $z$  ETGs we have found that only 4 galaxies out 11 have color gradients well reproduced by pure radial metallicity variation. Moreover, the metallicity gradients we have detected in high- $z$  ETGs ( $[-0.3$  to  $-1.45]$ ) are systematically steeper than those typically observed in local ETGs ( $[-0.16$  to  $-0.3]$ ), even if Ogando et al. (2005) found



that this range become wider ( $[0.0 \div -1.0]$ ) for nearby massive ( $M_* > 10^{10} M_\odot$ ) ETGs see also Spolaor et al. 2009). The steeper metallicity gradients that we have detected derive by a radial metallicity variation from supersolar ( $2Z_\odot$ ) values in the inner regions to subsolar values in the external regions ( $0.2Z_\odot$ ). Although such extreme values of  $Z$  have been observed also in few local ETGs (Mehlert et al. 2003; Rickes et al. 2008), our results show that metallicity gradients in high- $z$  ETGs of our sample are only marginally comparable with the typical metallicity gradients detected in local ETGs. This result seems to point in favor of a possible evolution of the metallicity gradient in the last 9Gyr.

Concurrently, studies on cluster ETGs at low and intermediate redshift show that pure age variations in their stellar populations are not able to account for their color gradients (Saglia et al. 2000). In contrast to local results, we have found that for  $\sim 50\%$  of the galaxies of our sample a radial variation of stellar populations age alone can reproduce the observed color gradients and global SED. In fact, recent studies investigating the simultaneous radial variation of both age and metallicity confirm metallicity gradients ( $\sim 0.4$  dex per radial decade) as the main driver of observed color gradients in local ETGs but found also a small contribution to color variation of positive age gradient ( $\sim 0.1$  dex per radial decade) (La Barbera & de Carvalho 2009; Wu et al. 2005). The age/metallicity degeneracy affecting optical colors does not allow us to consider the simultaneous radial variation of both parameters and hence to detect a possible positive age gradient, whose presence in local ETGs, actually, is still matter of debate.

To spread light on this issue, high- $z$  ETGs constitute the ideal place to investigate the presence of an age gradient. Indeed, at fixed radial variation of age  $\Delta\text{age}$ , its effect on color profile is much more enhanced when stellar populations are younger, hence in high- $z$  ETGs. This effect is clearly shown in left panel of Fig. 11, where we report the differences observed in the F850LP-F160W color of two stellar populations with age which differ of 2Gyr ( $\tau = 0.1\text{Gyr}$ , black solid curve), as a function of the age of the youngest stellar population. The same  $\Delta\text{age}$  produces a difference in the F850LP-F160W color of the two populations that is  $\sim 10$  times higher if observed in high- $z$  ETGs (Age  $< \sim 4\text{Gyr}$ ) respect those observed in local ETGs (Age  $\sim 10\text{Gyr}$ ). A typical radial variation of 2 Gyr, as the one we measure in the ETGs of our sample, will produce in a local ETG a variation in the F850LP-F160W color of  $\sim 0.05$  mag, thus at the very limit of the detection. On the contrary, the same age variation will result in a color variation of  $\sim [0.3-0.5]$  mag for high- $z$  ETGs. Red and blue lines report the same of black line, but for pure metallicity variations. In particular, red line show the variation in the F850LP-F160W color observed in two populations with metallicities  $2Z_\odot$  and  $0.2Z_\odot$ , while blue line in two populations with metallicities  $Z_\odot$  and  $0.2Z_\odot$ . In the right panel of Fig. 11 the color gradient that the above age/metallicity variations would produce when occurring between  $0.1R_e$  and  $3R_e$ . Differently from age variation, the effect of a metallicity variation on color, and hence on gradient, increases with the age of the galaxy of a factor  $\sim 2$  from high- $z$  ETGs to local ETGs. These plots emphasize how challenging is the detection of an age gradient in local ETGs due to its almost negligible effect on color profile. On the contrary, in high- $z$  ETGs age and metallicity variations

produce comparable effect on color profile, thus setting the ideal condition for their detection. This comparison with local samples is only meant to have an indication on how the results obtained at high- $z$ , both in terms of age/ $Z$  gradients and in terms of internal and external age/ $Z$  values, relate with the local values. On the other hand, the unknown evolution experienced by ETGs in  $\sim 9$  Gyr from  $z \sim 1.5$  to  $z=0$  can affect the stellar properties and distribution (e.g. minor mergers triggering secondary burst of star formation) making complex any comparison with local universe. In fact, to properly face on high- $z$  and local values samples of ETGs selected in an homogeneous way, a dataset able to trace the evolution of the same rest-frame color gradient over 9 Gyr, and similar procedures for both the color gradients estimates and the relative analysis should be considered. In a forthcoming paper, taking into account all these factors, we will try to address the origin of the color gradients following their evolution from  $z \sim 2$  to  $z=0$ .

For the remaining five ETGs of our sample, a pure radial variation of a single stellar population parameter is not able to reproduce the observed color gradients and global SEDs. Differently from the previous cases, where color gradients could be reproduced by a pure age or metallicity gradient as well as by a simultaneous radial variation of more than one parameter, these galaxies *need* a more complex scenario whereby more than one property of the stellar populations have to vary from the center to the periphery to generate the observed color gradients.

Thus, our analysis clearly indicates that the properties of the stellar population and their distribution within high- $z$  ETGs do not follow an homogeneous and common scheme.

In the following we try to investigate if the theoretical expectations of the widely accepted scenarios of galaxy formation can explain the observed color distributions.

In the monolithic revised scenario, color gradients are supposed to be mainly due to metallicity gradient, being the contribution of age null or mild (and positive). Our findings of none correlation between color/metallicity gradients and total mass suggest that the monolithic revised scenario is not the favored mechanisms with which ETGs assembled their mass, although the narrow mass range covered and the assumption of the stellar mass as a proxy of the total stellar mass can affect this conclusion.

Theoretical predictions of the *inside-out-growth* scenario point in favor of compact ETGs with cores (Wuyts et al. 2010) redder than the outskirt regions. This negative color gradient seems to be due to a combined effect of negative metallicity and positive age gradients, with a non negligible effect of dust (Wuyts et al. 2010). To compare our results with the theoretical prediction of this model, we define compact galaxies those ETGs with effective radius more than  $1\sigma$  smaller than those predicted by the local size-mass relation (SMR) for that mass. In Table 3 we report the compactness  $C$  for the galaxies of our sample defined as the ratio  $R_{e,z=0}/R_e$  where  $R_e$  is the effective radius of the galaxy and  $R_{e,z=0}$  is the radius that a galaxy of equal stellar mass would have at  $z=0$  as derived by the SMR of Shen et al. (2003). In our sample, compact galaxies, as we defined them, turn out to have  $C \geq 2$ . In Fig 12 we report the SMR in the F850LP band for our sample (solid symbols) and for local galaxies (solid line, Shen et al. 2003). The dashed lines represent the scatter at  $1\sigma$ . It turns out that seven out of 11 galaxies (solid

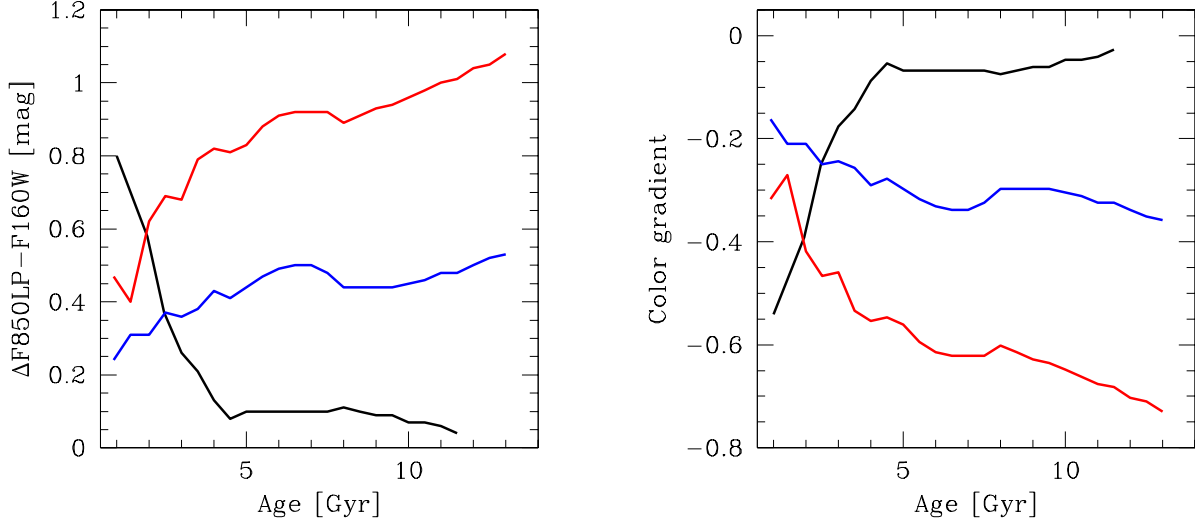


**Figure 11.** *Left panel:* Black line shows the difference observed in the F850LP-F160W color of two stellar populations with age differentiating of 2Gyr, as a function of the age of the youngest stellar population. Red line shows the variation in the F850LP-F160W color observed in two populations with metallicities  $2Z_{\odot}$  and  $0.2Z_{\odot}$ , while blue line for two populations with metallicities  $Z_{\odot}$  and  $0.2Z_{\odot}$ . *Right panel* Color gradients relative to the color variation in the left panel in the hypothesis that they occur between  $0.1R_e$  and  $3R_e$ .

points) of our sample are compact (magenta points) and 4 are normal ETGs (cyan triangles). In Table 3, we report the classification in normal (N) and compact (C) for our galaxies. Compact ETGs in our sample (as well as normal ETGs) show redder cores supporting the *inside-out-growth* scenario even if we cannot firmly establish the origin and the nature of this gradient. Actually, we cannot test the presence of a positive age gradient, since due to age/metallicity degeneracy we do not treat the case of simultaneous radial variation of age and metallicity. On the other hand, our results show that only two out of seven compact ETGs have color gradients well reproduced by a metallicity gradient.

Nonetheless, the simulations predicts that the negative color gradients produced by the interplay of age, metallicity and dust should result to correlate with the integrated rest-frame optical color. Following Wuyts et al. (2010) in Fig. 13 we show the ratio between the F850LP-band effective radius and F160W-band effective radius as a proxy of the color gradients versus the F850LP-F160W color. The points follow the same convention of Fig. 12. We do not find any correlation neither in the whole sample, nor in the compact selection. The absence of such correlations cast some doubts on the validity of this scenario as a viable process to assemble the stellar mass in compact ETGs.

Despite the fact that both the widely accepted formation scenarios do not seem to be able to reproduce the stellar content of high- $z$  ETGs, we have to test the hypothesis whether ETGs can be assembled through a common formation process and the distribution we observed in color gradients can be the final product of subsequent merger events. We have to bear in mind that our galaxies are all younger than 3.5 Gyr. This severely constrains the time each galaxy has at disposal to experience a merger event. Table 1 of

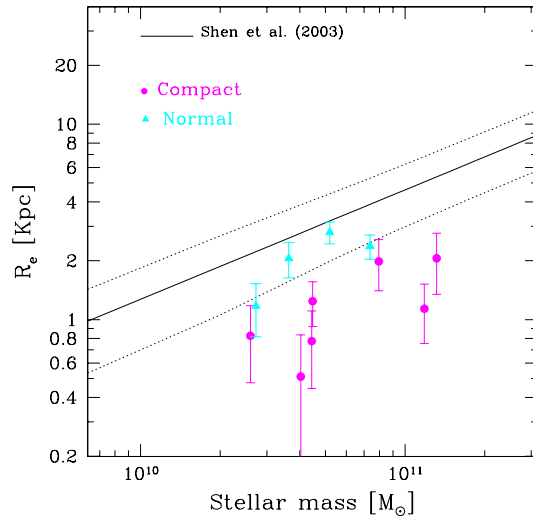


**Figure 12.** SM relation for local ETGs (solid line, Shen et al. 2003) and for our sample (solid symbols). The dashed lines are the scatter lines at  $1\sigma$ . We shifted the Shen et al.s relation by a factor 1.2 towards lower masses to take into account the systematic shift observed in the mass estimations using our models or those adopted by Shen et al. (2003). The circles are compact galaxies, that is, galaxies having the effective radius more than  $1\sigma$  smaller than those predicted by a local relation for that mass. On the contrary, galaxies having the effective radius comparable at  $1\sigma$  with those expected by Shen et al.s relations are classified as normal (triangle symbols).

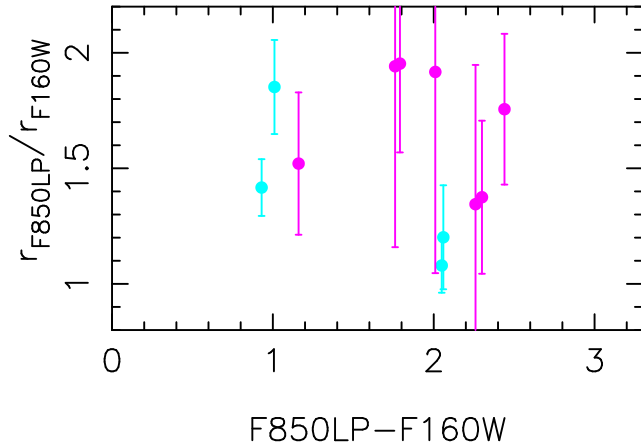


**Figure 13.** The  $r_{e,F850LP}/r_{e,F160W}$  ratio as proxy of F850LP-F160W color gradient vs the F850LP-F160W global color.

Boylan-Kolchin et al. (2008) shows the dynamical friction merging time in Gyr,  $\tau_{merger}$ , for a host halo with virial mass  $M_{host} = 10^{12}M_{\odot}$ , measured from numerical simulations. They assumed different initial orbital angular momentum, initial orbital energy, and ratio of initial satellite mass to initial host halo mass and only for two cases they found 3.5 Gyr is enough to complete the merger, while in all the other cases  $\tau_{merger}$  is greater than 4.3 Gyr. Thus, the different stellar content of high- $z$  ETGs does not seem to be due to the effect of subsequent merger events, but primarily to the formation process. Actually, the continuum distribution of ETGs in the size-mass plane, both at high redshift and in the local Universe, together with the systematic direction of the color gradient (negative or null) of high- $z$  ETGs, point toward a common formation process responsible of this continuity. The possible different initial conditions, such as the different time scale of collapsing gas cloud, can be responsible of the observed structural and dynamical differences as we previously suggested (Saracco et al. 2011, 2012).

## ACKNOWLEDGMENTS

This work is based on observations made with the ESO telescopes at the Paranal Observatory and with the NASA/ESA Hubble Space Telescope, obtained from the data archive at the Space Telescope Science Institute which is operated by the Association of Universities for Research in Astronomy. This work has received financial support from ASI-INAF (contract I/009/010/0) and from PRIN-INAF (1.05.01.09.05).

## REFERENCES

Bell E. F., Wolf C., Meisenheimer K., Rix H.-W., Borch A., Dye S., Kleinheinrich M., Wisotzki L., McIntosh D. H., 2004, *ApJ*, 608, 752  
 Bertin E., Arnouts S., 1996, *A&AS*, 117, 393  
 Bezanson R., van Dokkum P. G., Tal T., Marchesini D., Kriek M., Franx M., Coppi P., 2009, *ApJ*, 697, 1290  
 Bolzonella M., Miralles J.-M., Pelló R., 2000, *A&A*, 363, 476

Boylan-Kolchin M., Ma C.-P., Quataert E., 2008, *MNRAS*, 383, 93  
 Calzetti D., Armus L., Bohlin R. C., Kinney A. L., Koornneef J., Storchi-Bergmann T., 2000, *ApJ*, 533, 682  
 Casertano S., de Mello D., Dickinson M., Ferguson H. C., Fruchter A. S., Gonzalez-Lopezlira R. A., Heyer I., Hook R. N., Levay Z., Lucas R. A., Mack J., Makidon R. B., Mutchler M., Smith T. E., Stiavelli M., Wiggs M. S., Williams R. E., 2000, *AJ*, 120, 2747  
 Chabrier G., 2003, *PASP*, 115, 763  
 Daddi E., Renzini A., Pirzkal N., Cimatti A., Malhotra S., Stiavelli M., Xu C., Pasquali A., Rhoads J. E., Brusa M., di Serego Alighieri S., Ferguson H. C., Koekemoer A. M., Moustakas L. A., Panagia N., Windhorst R. A., 2005, *ApJ*, 626, 680  
 De Lucia G., Springel V., White S. D. M., Croton D., Kauffmann G., 2006, *MNRAS*, 366, 499  
 Dekel A., Birnboim Y., Engel G., Freundlich J., Goerdt T., Mumcuoglu M., Neistein E., Pichon C., Teyssier R., Zinger E., 2009, *Nature*, 457, 451  
 Di Matteo P., Pipino A., Lehnert M. D., Combes F., Semelin B., 2009, *A&A*, 499, 427  
 Gargiulo A., Saracco P., Longhetti M., 2011, *MNRAS*, 412, 1804  
 Giavalisco M., Ferguson H. C., Koekemoer A. M., Dickinson M., Alexander D. M., Bauer F. E., Bergeron J., Biagetti C., Brandt W. N., Casertano S., 2004, *ApJ*, 600, L93  
 Guo Y., Giavalisco M., Cassata P., Ferguson H. C., Dickinson M., Renzini A., Koekemoer A., Grogin N. A., Papovich C., Tundo E., Fontana A., Lotz J. M., Salimbeni S., 2011, *ApJ*, 735, 18  
 Hinkley S., Im M., 2001, *ApJ*, 560, L41  
 Hopkins P. F., Bundy K., Murray N., Quataert E., Lauer T. R., Ma C.-P., 2009, *MNRAS*, 398, 898  
 Idiart T. P., Michard R., de Freitas Pacheco J. A., 2003, *A&A*, 398, 949  
 Katz N., 1991, *ApJ*, 368, 325  
 Kawata D., 2001, *Apj*, 558, 598  
 Khochfar S., Silk J., 2006, *ApJ*, 648, L21  
 Kobayashi C., 2004, *MNRAS*, 347, 740  
 Koekemoer A. M., Fruchter A. S., Hook R. N., Hack W., 2002, in S. Arribas, A. Koekemoer, & B. Whitmore ed., *The 2002 HST Calibration Workshop : Hubble after the Installation of the ACS and the NICMOS Cooling System MultiDrizzle: An Integrated Pyraf Script for Registering, Cleaning and Combining Images.* p. 337  
 La Barbera F., de Carvalho R. R., 2009, *ApJ*, 699, L76  
 La Barbera F., de Carvalho R. R., Kohl-Moreira J. L., Gal R. R., Soares-Santos M., Capaccioli M., Santos R., Sant’anna N., 2008, *PASP*, 120, 681  
 Longhetti M., Saracco P., Severgnini P., Della Ceca R., Mannucci F., Bender R., Drory N., Feulner G., Hopp U., 2007, *MNRAS*, 374, 614  
 Mehlert D., Thomas D., Saglia R. P., Bender R., Wegner G., 2003, *A&A*, 407, 423  
 Merlin E., Chiosi C., 2006, *A&A*, 457, 437  
 Naab T., Johansson P. H., Ostriker J. P., 2009, *ApJ*, 699, L178  
 Nipoti C., Treu T., Auger M. W., Bolton A. S., 2009, *ApJ*, 706, L86  
 Oesch P. A., Bouwens R. J., Illingworth G. D., Carollo

- C. M., Franx M., Labbé I., Magee D., Stiavelli M., Trenti M., van Dokkum P. G., 2010, *ApJL*, 709, L16
- Ogando R. L. C., Maia M. A. G., Chiappini C., Pellegrini P. S., Schiavon R. P., da Costa L. N., 2005, *ApJ*, 632, L61
- Peletier R. F., Valentijn E. A., Jameson R. F., 1990, *A&A*, 233, 62
- Peng C. Y., Ho L. C., Impey C. D., Rix H., 2002, *AJ*, 124, 266
- Renzini A., 2006, *ARA&A*, 44, 141
- Rickes M. G., Pastoriza M. G., Bonatto C., 2008, *MNRAS*, 384, 1427
- Saglia R. P., Maraston C., Greggio L., Bender R., Ziegler B., 2000, *A&A*, 360, 911
- Salpeter E. E., 1955, *ApJ*, 121, 161
- Saracco P., Gargiulo A., Longhetti M., 2012, *ArXiv e-prints*
- Saracco P., Longhetti M., Gargiulo A., 2010, *MNRAS*, pp L115+
- Saracco P., Longhetti M., Gargiulo A., 2011, *MNRAS*, 412, 2707
- Shen S., Mo H. J., White S. D. M., Blanton M. R., Kauffmann G., Voges W., Brinkmann J., Csabai I., 2003, *MNRAS*, 343, 978
- Spolaor M., Proctor R. N., Forbes D. A., Couch W. J., 2009, *ApJ*, 691, L138
- Tamura N., Ohta K., 2003, *AJ*, 126, 596
- Toomre A., Toomre J., 1972, *Apj*, 178, 623
- Vanzella E., Cristiani S., Dickinson M., Giavalisco M., Kuntschner H., Haase J., Nonino M., Rosati P., Cesarsky C., Ferguson H. C., GOODS Team 2008, *A&A*, 478, 83
- Windhorst R. A., Cohen S. H., Hathi N. P., McCarthy P. J., Ryan Jr. R. E., Yan H., Baldry I. K., Driver S. P., Frogel J. A., Hill D. T., Kelvin L. S., Koekemoer A. M., 2011, *ApJS*, 193, 27
- Wu H., Shao Z., Mo H. J., Xia X., Deng Z., 2005, *ApJ*, 622, 244
- Wuyts S., Cox T. J., Hayward C. C., Franx M., Hernquist L., Hopkins P. F., Jonsson P., van Dokkum P. G., 2010, *ApJ*, 722, 1666

MATERIAL PRESENTED IN ELECTRONIC FORM

Galaxy #2111

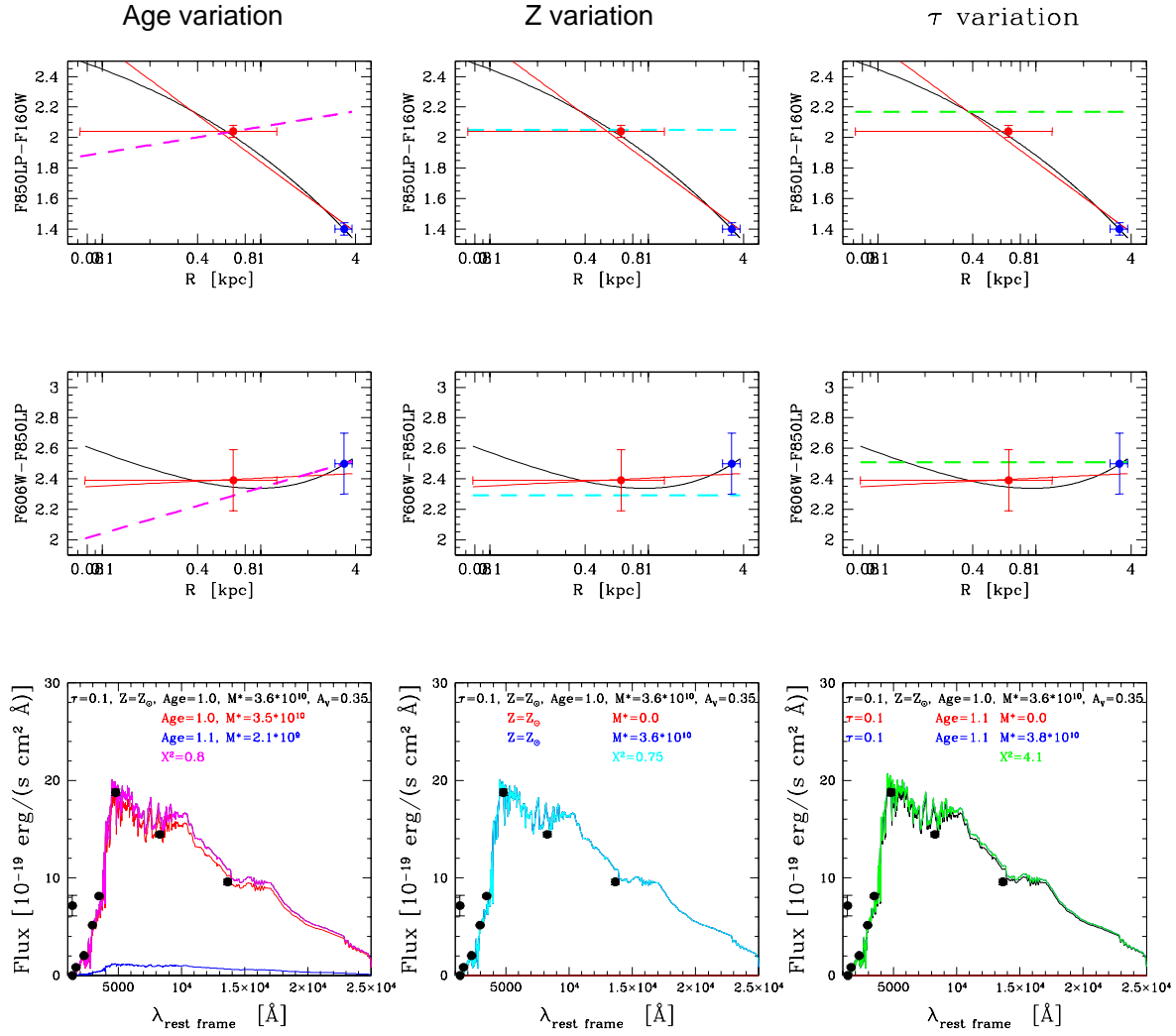


Figure 7. (continued)

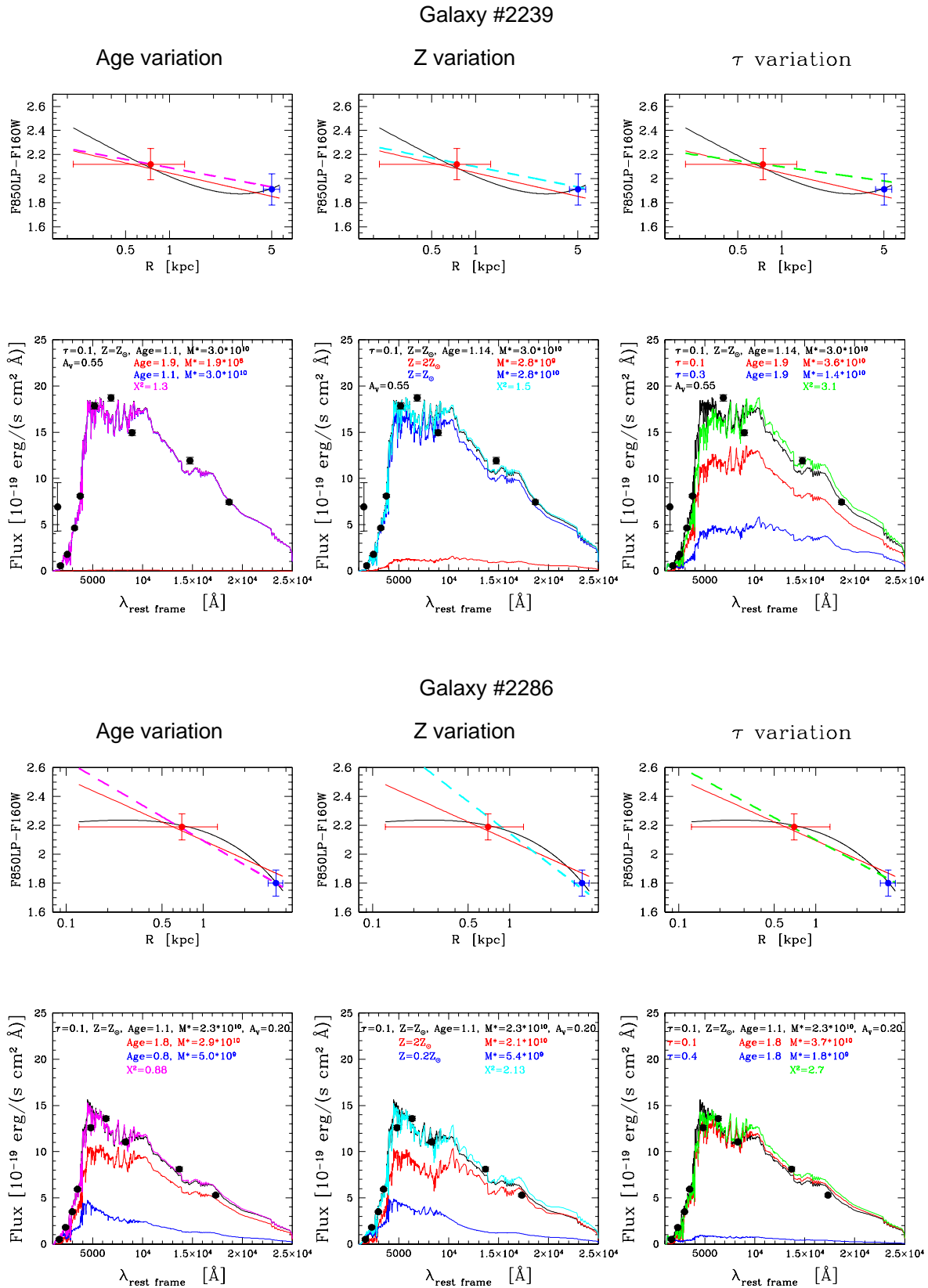


Figure 7. (continued)

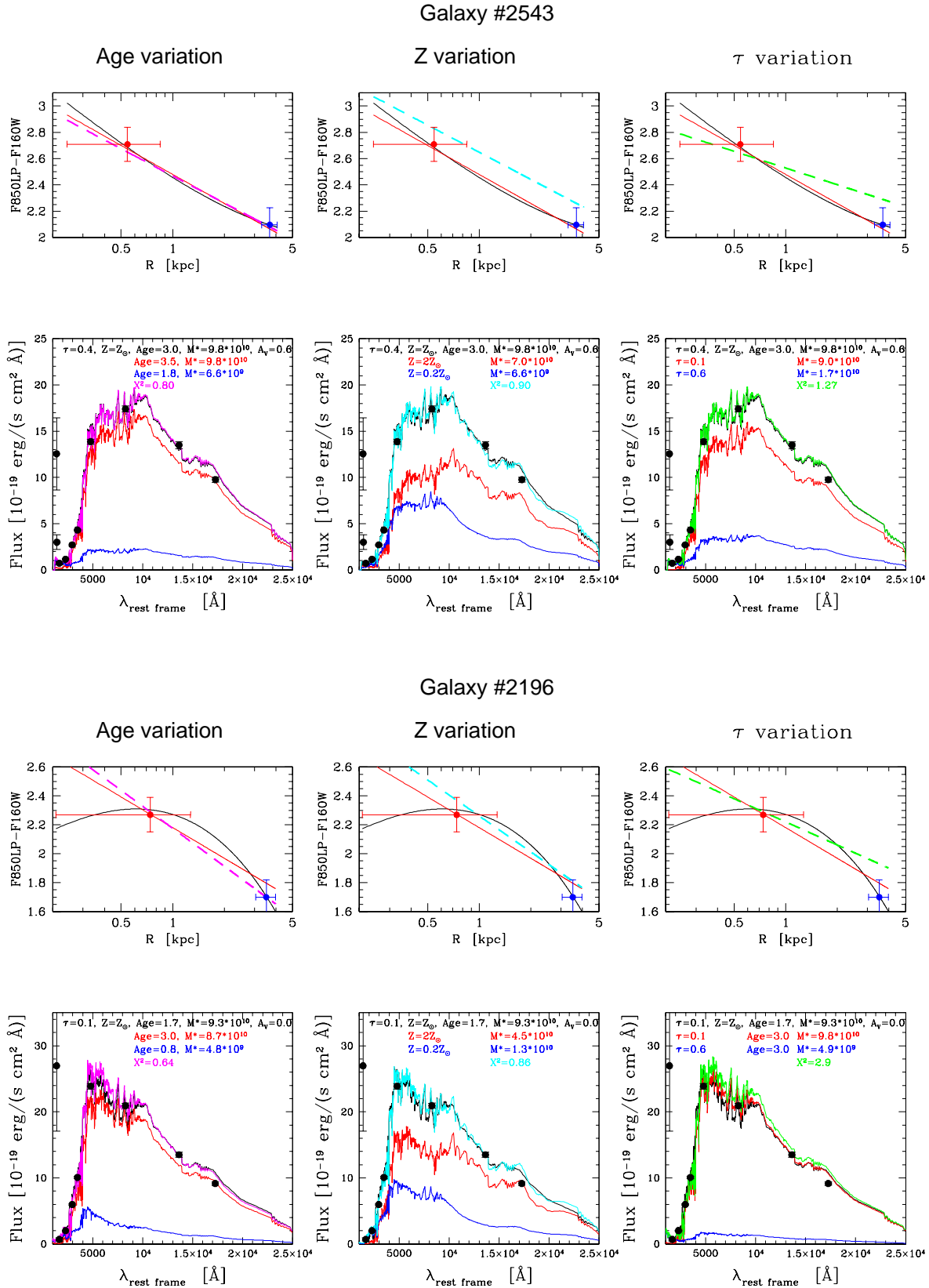


Figure 7. (continued)



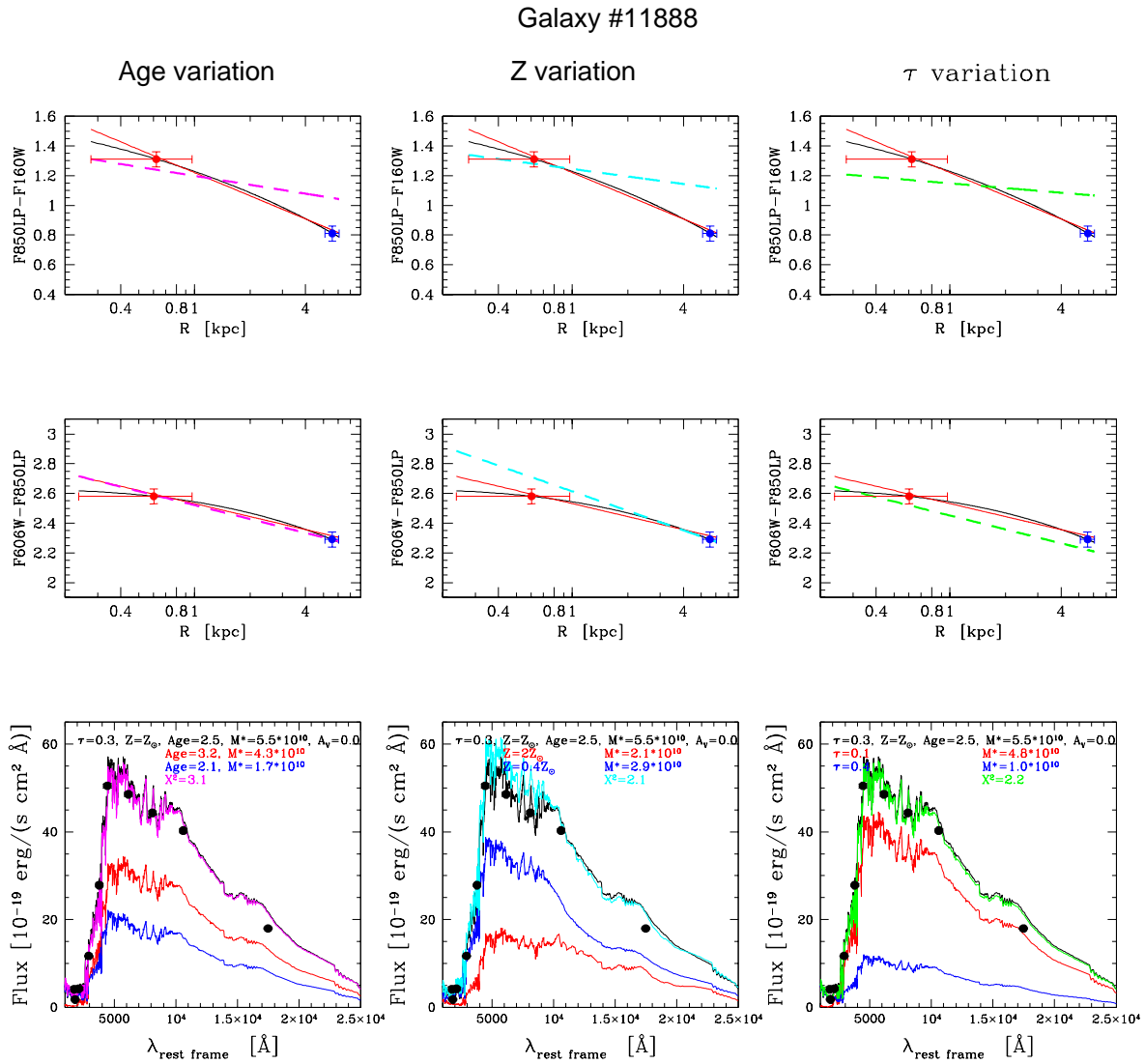


Figure 7. (continued)

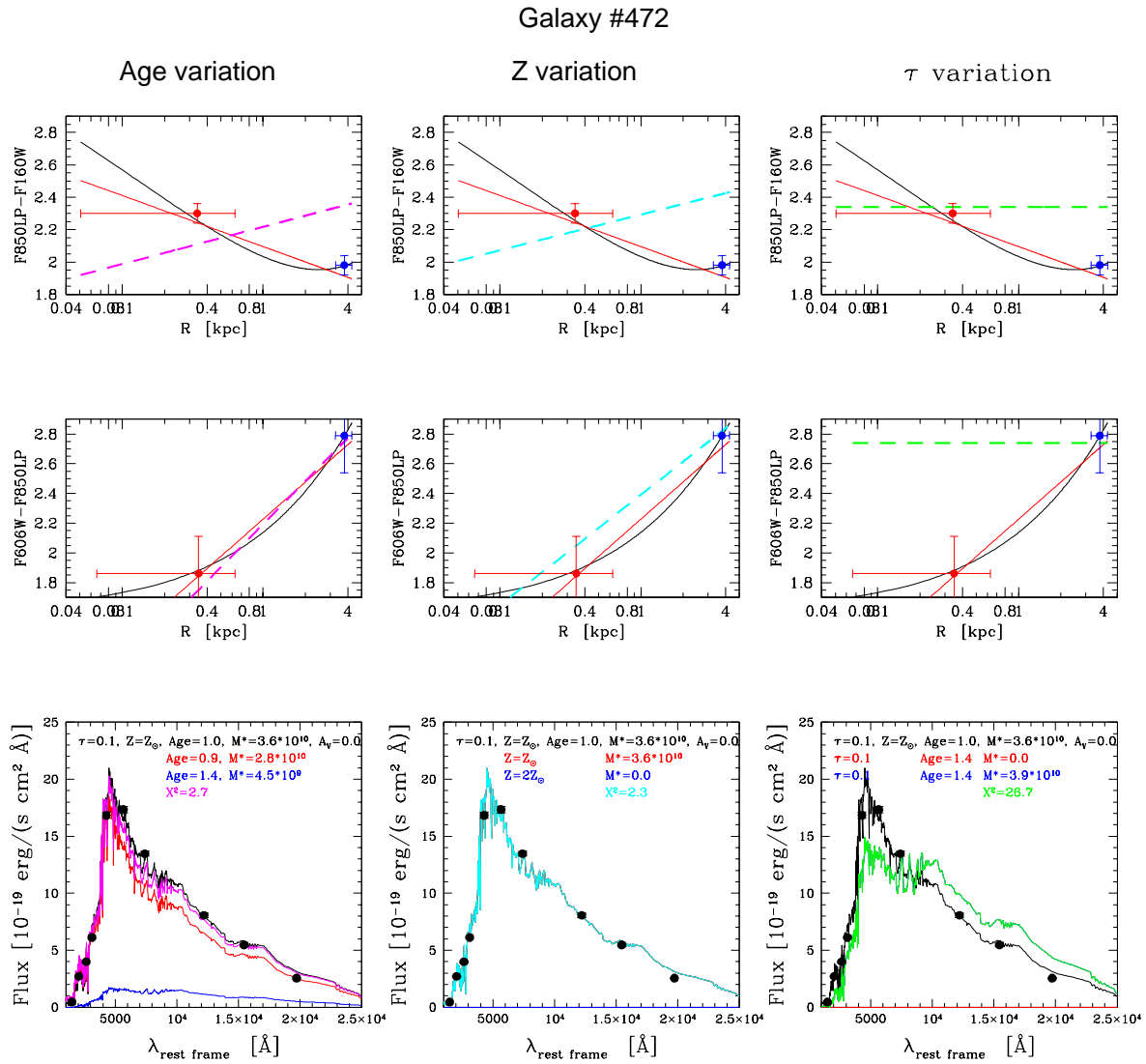


Figure 7. (continued)

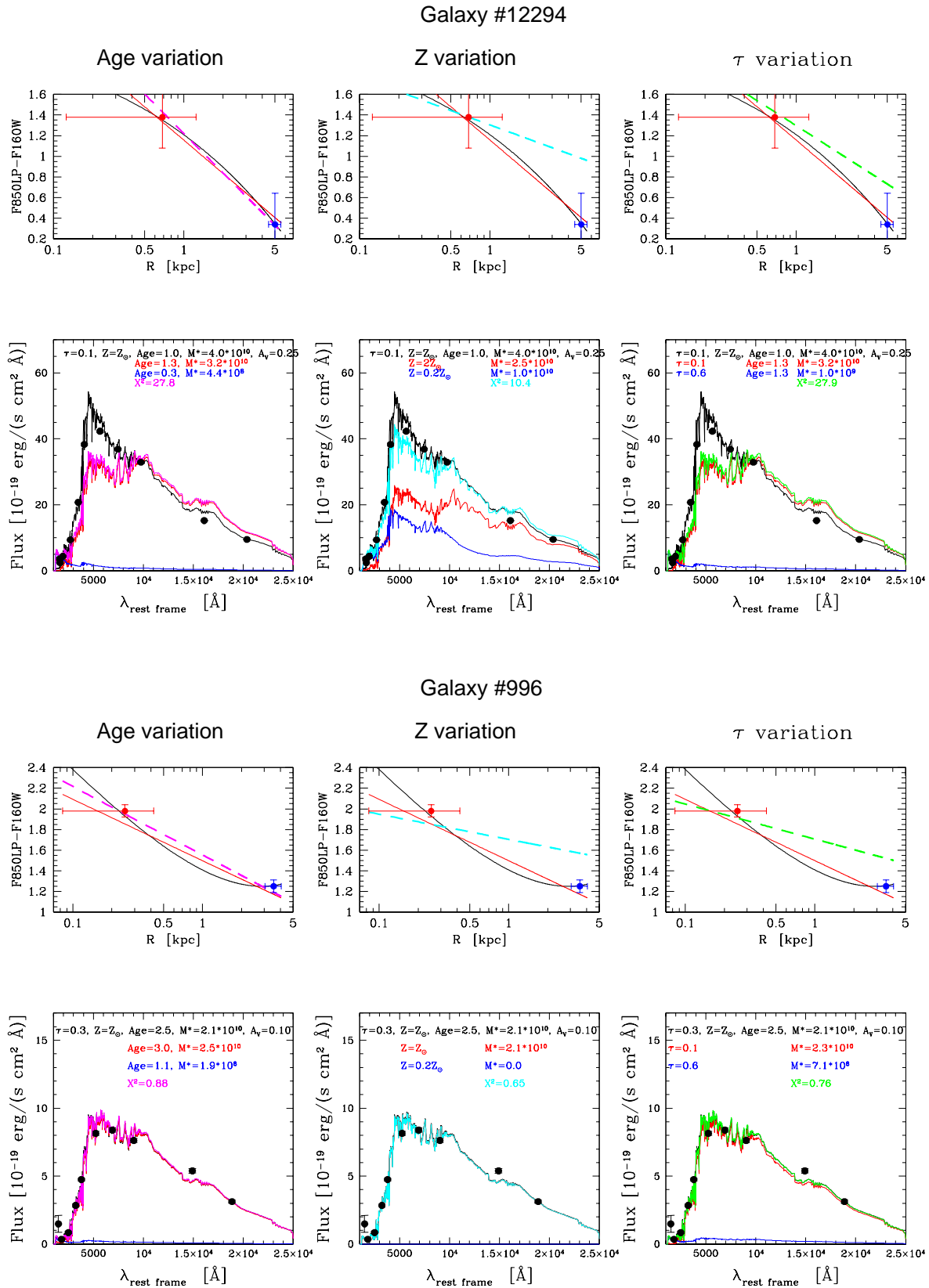


Figure 7. (continued)

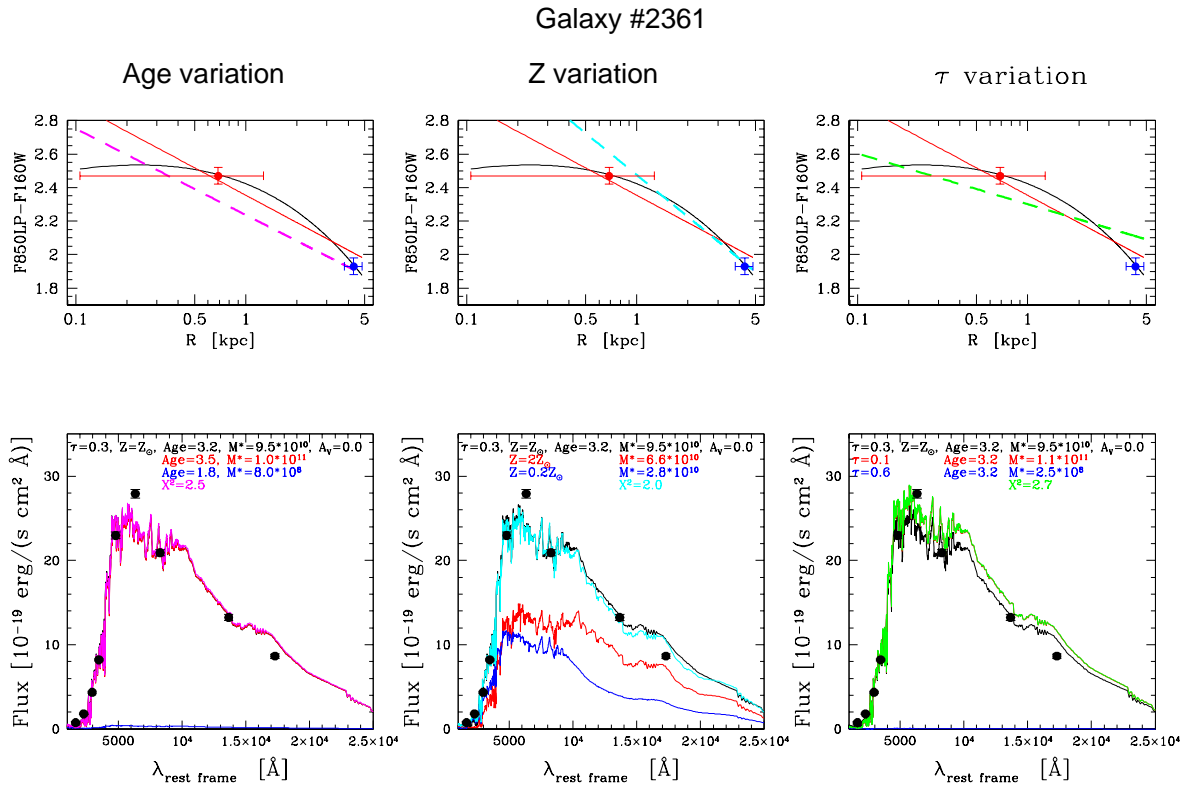
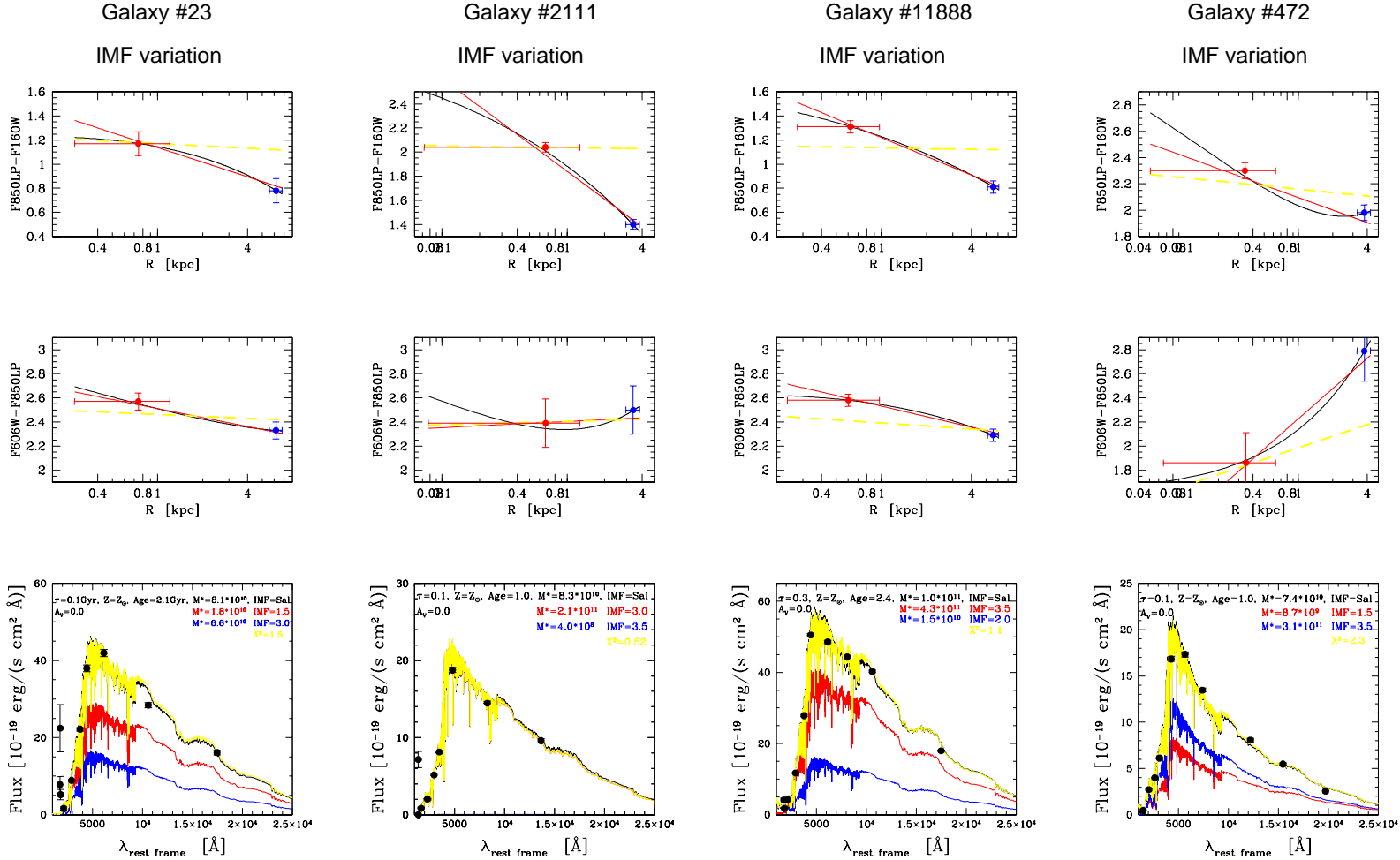


Figure 7. (continued)



**Figure 10.** Analysis of the radial variation of IMF's slope as possible driver of observed color gradients. Top and middle panels show the F850LP-F160W and F606W-F850LP color profiles, respectively (black lines), with the relative fit (red lines). The bottom panel shows the observed global SED (black dots) as well as the stellar population parameters (black text) derived from its fit (black line) assuming a Salpeter IMF. Among all the stellar populations with varying IMF's slope but age, star-formation time scale, metallicity and dust extinction equal to the value obtained from the fit of the global SED, the red text identifies the one that best simultaneously reproduces the colors observed in the internal region (red dots in the top and middle panel). Similarly, blue text reports the value of the slope of the IMF that best reproduce the external colors (blue dots in the upper panels). The pure linear variation of the IMF's slope from the internal value to the external one, will produce the F850LP-F160W and F606W-F850LP color gradients represented with the dashed yellow lines. The contribution to the total stellar mass of the two populations is fixed in order to best fit the whole SED and are reported in the bottom panel (red and blue lines).

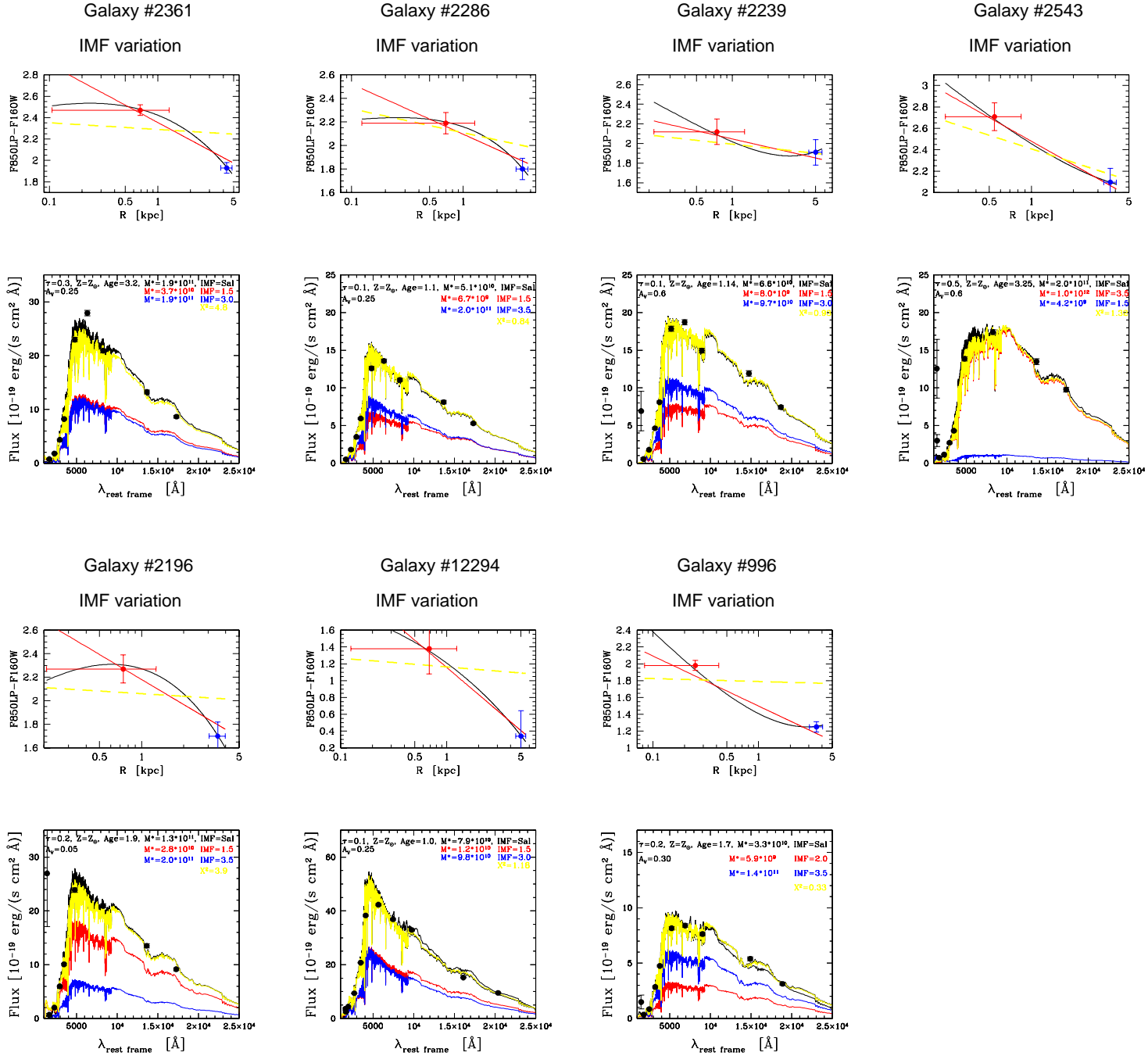


Figure 10. (continued)